UNIVERSIDADE
BEIRA INTERIOR

Turbulence Modelling on Supercritical Jet Injection

Francisco Miguel Marques de Carvalho

Dissertação para obtenção do Grau de Mestre em
Engenharia Aeronáutica
ciclo de estudos integrado

versão final após defesa

Orientador: Prof. Doutor André Resende Rodrigues da Silva

Julho 2020

Acknowledgments

I start by thanking my supervisor Prof. Dr. André Silva for sparking my interest in the field of fluid dynamics a few years ago with his lessons and for creating the amazing environment that allowed me to write this work during the last few months surrounded not only by supporting people but also humour and friendship. The second person that was vital to this work was Leandro Magalhães. Thank you for bringing me up to speed with the world of CFD and later on for the continued advice and great insight. A big thank you also for proof-reading this work and all the suggestions.

Filipa, Daniel and Inês, thank you for the fun you have brought me not only during work time but also after hours. I have had some great laughs thanks to you. This, of course, extends itself to the remaining friends with whom I shared an office. Even if I didn't talk so much, I was often silently laughing in my chair.

I would also like to thank one of my closest friends, Gustavo, for the very interesting and almost daily discussions about each other's works. They shaped my thoughts and ultimately this study. Next to him, I also want to thank Filipe, Luís, António and Rui not only for constantly putting up with me but also for their friendship that will for sure last for a lifetime.

In the end, I must thank my family without whom I would not be where I am today. To André and Afonso for their love and company, that I know will be with me as long as I live. To my grandparents, Lucete and Francisco, who have always shared with me not only their support and affection but also the best meals in the world. Finally to my mother, Isabel, and my father, Carlos, for raising me to be inquisitive about everything, rigorous with myself and patient with others. Thank you for the sacrifices you have made to give me this opportunity. I will always remember that and work to make you proud.

Resumo

A passagem do sector privado de segundo para primeiro plano, no campo da exploração espacial depende, em grande parte, da viabilidade financeira de tais projetos. É difícil de estimar até que ponto este sector conseguirá desenvolver os recursos já disponíveis para a exploração espacial, mas a ligação entre avanço tecnológico e redução de custos é inquestionável.

Em motores foguete de propelente líquido, uma combustão mais eficiente implica uma transição do combustível e/ou oxidante para o regime supercrítico. Apesar de estas condições não serem novidade dentro da câmara de combustão de um motor foguete, ainda não são perfeitamente compreendidas e as ferramentas para as estudar ainda estão em fase de desenvolvimento.

O comportamento não linear das propriedades termofísicas de um fluido no regime supercrítico aumenta a dificuldade de qualquer simulação numérica nestas condições. Neste trabalho, a lei dos gases ideais perde validade e é substituída por modelos de maior precisão. As Equações de Estado de Peng-Robinson e de Soave-Redlich-Kwong são comparadas com uma Equação de Estado multiparamétrica de referência para o azoto, permitindo assim estimar o erro associado a cada um destes modelos. Esta Equação de Estado de referência é implementada através da base de dados REFPROPv9.1 que oferece simultaneamente um aumento de precisão e redução de custo computacional. O mesmo cuidado é também aplicado às propriedades calóricas e de transporte.

Para lidar com o escoamento incompressível, mas de massa específica variável, dentro da câmara de combustão, a média normalmente aplicada às equações de conservação de massa, quantidade de movimento e energia é dispensada em favor da média de Favre, ponderada pela massa específica. Este sistema de equações é por fim fechado com diferentes modelos de turbulência, onde reside o principal foco deste estudo. O desempenho e a validade de tais modelos, desenvolvidos e calibrados para condições subcríticas, são estudados para condições supercríticas.

Por fim, os dados experimentais correspondentes ao desenvolvimento de camada de mistura de azoto são usados para validação. Os resultados mostram-se em boa concordância com os experimentais e, quando comparados com os de outros estudos numéricos semelhantes, mostram que não existe, de facto, uma dependência monotónica entre a complexidade de um modelo de turbulência, desempenho e qualidade de resultados.

Palavras-chave

injeção em condições supercríticas, modelo de turbulência, equação de estado, motores foguete

Abstract

As space exploration enters a new era where not only public but also private enterprises begin to flourish, financial viability becomes a preponderant factor. It is hard to estimate how far the contribution of this sector to the development of the resources available thus far will be, but the link between engineering technology and cost reduction is unquestionable.

In a Liquid Rocket Engine, higher combustion efficiency comes at the cost of both the fuel and/or the oxidiser surpassing their critical points and entering the domain of supercritical fluids. While these conditions have been present in rocket engines combustion chambers for decades, they are still not fully understood and tools to properly simulate such conditions are still in the development stages.

The highly non-linear behaviour of the thermophysical properties of a fluid in this regime increases the difficulty of any attempt to run numerical simulations. The ideal gas law is no longer valid and must be replaced by more accurate models. The Peng-Robinson and the Soave-Redlich-Kwong Equations of State (EoS) are compared to a reference EoS for nitrogen to gain some insight on the magnitude of error that simpler cubic Equations of State incur in the simulation results. The output of the multi-parameter EoS is obtained from the real gas library REFPROPv9.1 thus reducing computational costs while still achieving a level of accuracy that would otherwise not be possible. A similar treatment must be given to transport and caloric properties that have a significant impact on the flow structure.

To deal with the incompressible but variable density conditions inside the combustion chamber, the standard time-averaging method is replaced by the Favre averaging procedure and the system of equations is closed with different turbulence models, the main focus of this study. The performance of said models, designed and calibrated to run in subcritical conditions, is then studied and their validity for the supercritical regime is assessed.

Ultimately, computational results are validated against experimental data regarding the development of the mixing layer of nitrogen. Results show a good agreement with experimental data and, when compared to additional numerical studies for the same conditions, it is visible that there is no monotonic dependence between model complexity, performance and quality of results.

Keywords

supercritical injection, turbulence model, Equation of State, Liquid Rocket Engine

Contents

List of Figures

List of Tables

Nomenclature

Kn	Knudsen Number	-
Re	Reynolds Number	-
Pe	Péclet Number	-
Pr	Prandtl Number	-
c_p	Isobaric Specific Heat	$[\mathrm{J \cdot kg^{-1} \cdot K^{-1}}]$
c_v	Isochoric Specific Heat	$[\mathrm{J \cdot kg^{-1} \cdot K^{-1}}]$
γ	Adiabatic Index	-
R	Real Gas Constant	$[\mathrm{J \cdot mol^{-1} \cdot K^{-1}}]$
F	Thrust, Helmholtz Energy, Flux	[N], [J], -
f	Non-Dimensional Helmholtz Energy	-
$\dot{m}$	Mass Flow Rate	$[\mathrm{kg \cdot s^{-1}}]$
m_p	Mass of Propellant	[kg]
A_e	Nozzle Exit Cross-Section	$[\mathrm{m^2}]$
I_{sp}	Specific Impulse	[s]
I_t	Total Impulse	$[\mathrm{N \cdot s^{-1}}]$
t_b	Burn Time	[s]
g_0	Standard Surface Gravity	$[\mathrm{m \cdot s^{-2}}]$
p	Pressure	[MPa]
ρ	Density	$[\mathrm{kg \cdot m^{-3}}]$
δ	Reduced Density	-
T	Temperature	[K]
τ	Inverse Reduced Temperature	-
x	Spatial Coordinate	[m]
u	Velocity	$[\mathrm{m \cdot s^{-1}}]$
u_t	Friction Velocity	$[\mathrm{m \cdot s^{-1}}]$
I	Raman Signal Intensity, Turbulent Intensity	-, -
Θ	Control Volume	$[\mathrm{m^3}]$
S	Control Surface	$[\mathrm{m^2}]$
σ_{ij}	Internal Stress Tensor	[MPa]
t_{ij}	Viscous Shear Stress Tensor	[MPa]
s_{ij}	Strain-Rate Tensor	$[\mathrm{s^{-1}}]$
$\tilde{S}_{ij}$	Mean Strain-Rate Tensor	$[\mathrm{s^{-1}}]$
$\tilde{S}$	Mean Strain-Rate Magnitude	$[\mathrm{s^{-1}}]$
ω_{ij}	Vorticity-Tensor	$[\mathrm{s^{-1}}]$
$\tilde{\Omega}_{ij}$	Mean Vorticity Tensor	$[\mathrm{s^{-1}}]$
$\tilde{\Omega}$	Mean Vorticity Magnitude	$[\mathrm{s^{-1}}]$
ϕ	Arbitrary Scalar	-
Γ	Diffusivity Coefficient	-
Q	Source Term	-

f_i	Body-Force Density Vector	$[\mathrm{N} \cdot \mathrm{m}^{-3}]$
h	Specific Enthalpy	$[\mathrm{J} \cdot \mathrm{kg}^{-1}]$
H	Total Specific Enthalpy	$[\mathrm{J} \cdot \mathrm{kg}^{-1}]$
e	Internal Specific Energy	$[\mathrm{J} \cdot \mathrm{kg}^{-1}]$
E	Total Specific Energy	$[\mathrm{J} \cdot \mathrm{kg}^{-1}]$
q	Heat Flux	$[\mathrm{J} \cdot \mathrm{s}^{-1}]$
κ	Thermal Conductivity	$[\mathrm{W} \cdot \mathrm{m}^{-1} \cdot \mathrm{K}^{-1}]$
α	Thermal Diffusivity	$[\mathrm{m}^2 \cdot \mathrm{s}]$
μ	Dynamic Viscosity	$[\mathrm{Pa} \cdot \mathrm{s}]$
ν	Kinematic Viscosity	$[\mathrm{m}^2 \cdot \mathrm{s}]$
$\tilde{\nu}$	Modified Turbulent Viscosity	$[\mathrm{m}^2 \cdot \mathrm{s}]$
δ_{ij}	Kronecker Delta Function	-
τ_{ij}	Reynolds Stress Tensor	[MPa]
k	Turbulent Kinetic Energy	$[\mathrm{m}^2 \cdot \mathrm{s}^{-2}]$
ε	Turbulent Dissipation Rate	$[\mathrm{m}^2 \cdot \mathrm{s}^{-3}]$
ω	Specific Dissipation Rate, Acentric Factor	$[\mathrm{s}^{-1}]$, -
l	Length Scale	[m]
l_{mix}	Mixing Length	[m]
d	Distance to Wall	[m]
v	Molar Volume	$[\mathrm{m}^3 \cdot \mathrm{mol}^{-1}]$
M	Molar Mass	$[\mathrm{g} \cdot \mathrm{mol}^{-1}]$
h_f	Heat Transfer Coefficient	$[\mathrm{W} \cdot \mathrm{m}^{-2} \cdot \mathrm{K}^{-1}]$
θ	Explicit Under-Relaxation Factor	-
φ	Velocity Potential	$[\mathrm{m}^2 \cdot \mathrm{s}]$
$\mathrm{x/d}$	Axial Coordinate Normalised by the Injector Diameter	-
$\mathrm{x_i}$	Injector Length	[m]
r	Radius	[m]
Δt	Time Interval, Pseudo-Time Relaxation Factor	[s], -
Δx	Spatial Interval	[m]

Subscripts

e	Nozzle Exit
cc	Combustion Chamber
0	Injection
∞	Farfield, Background
c	Critical
w	Wall
S	Surface
V	Volume
eff	Effective
A	Advective
D	Diffusive
i, j, k, x, y, z	Cartesian Directions
$\tilde{\nu}, k, \varepsilon, \omega$	Turbulent Properties

Superscripts

$+$	Normalised
0	Ideal Contribution
r	Residual Contribution
$\tilde{\phi}$	Favre Average
$''$	Favre Fluctuation
$\overline{\phi}$	Reynolds Average
$'$	Reynolds Fluctuation

Additional Equation of State Parameters

a, b
ζ, m
$a_1, a_2, a_3, a_3, a_4, a_5, a_6, a_7, a_8$
$N_k, i_k, j_k, l_k, \phi_k, \beta_k, \gamma_k$
$\Phi, \hat{\Phi}, \hat{\Phi}_0$
σ, T^*, θ
$q_D, k_B, R_0, \xi, \xi_0, \tilde{\chi}$
$\Gamma, \gamma, \mathrm{v}$

Additional Turbulence Modelling Parameters

f_{v1}, f_{v2}
$\chi, \chi_k, \chi_\omega$
P, D
g, r
$\psi, \psi_0, \psi_k, \psi_\varepsilon$
$C_1, \tilde{C}_{\varepsilon 2}, \lambda$
A_s, U^*, ξ, η
f_{β^*}, f_β
$\theta_{Total}, \theta_1, \theta_2$
$F_1, F_2, \mathrm{arg}_1, \mathrm{arg}_2, CD^+$
$\Pi_{ij}, \varepsilon_{ij}, C_{ijk}$
$\hat{\alpha}, \hat{\gamma}, P_{ij}, D_{ij}$
$u^*, T_f, \hat{S}, \gamma, c_{w1}$

Turbulence Modelling Coefficients

$c_{w2}, c_{w3}, c_{v1}, c_{b1}, c_{b2}$
$\sigma_k, \sigma_{k1}, \sigma_{k2}$
$\sigma_\omega, \sigma_{\omega 1}, \sigma_{\omega 2}$
$\sigma_\varepsilon, \sigma_{\tilde{\nu}}$
$C_\mu, C_{\varepsilon 1}, C_{\varepsilon 2}, C_2$
A_0, λ_0
$\beta^*, \beta, \beta_1, \beta_2$
κ

List of Acronyms

BSL	Baseline
BWR	Benedict-Webb-Rubin
CFD	Computational Fluid Dynamics
DLR	Deutsches Zentrum für Luft- und Raumfahrt
DNS	Direct Numerical Simulation
EWT	Enhanced Wall Treatment
EoS	Equation of State
FVM	Finite Volume Method
FWHM	Full Width Half Maximum
LES	Large Eddy Simulation
LRE	Liquid Rocket Engine
MBWR	Modified Benedict-Webb-Rubin
NIST	National Institute of Standards and Technology
PR	Peng-Robinson
QUICK	Quadratic Upstream Interpolation for Convective Kinematics
REFPROP	Reference Fluid Thermodynamic and Transport Properties Database
SST	Shear Stress Transport
SRK	Soave-Redlich-Kwong
UDF	User Defined Function

Chapter 1

Introduction

Supercritical fluids exist as a byproduct of different natural occurring phenomena. In submerged volcanos, for example, pressure crosses the critical point for water at around $2200\,\mathrm{m}$ below sea level and together with the high temperatures of a volcanic eruption, the liquid water turns into a gas-like fluid, triggering underwater lava fountains [1]. The atmosphere of Venus is another example. It is mostly comprised of CO_2 meaning that, for its temperatures and pressures values, it is in the supercritical regime [2, 3].

In the industry, the applications for such fluids seem to be never-ending, ranging from supercritical drying used to produce aerogels to the extraction of substances and cleaning processes where there is also an apparent ecological benefit [4]. Its appearance in propulsion has become more noticeable with the development of higher pressure systems such as when diesel is compressed in an internal combustion engine [5, 6], but the scope of this work falls on a different system.

Rocket engines are mainly used to launch vehicles into space, where atmospheric propulsion systems are not appropriate. The principle is that of expelling accelerated mass and, through Newton's third law, using the resulting reaction force as thrust. This is similar to how a jet engine works, except that rocket engines must carry both their fuel and oxidiser. The chemical reaction between the propellants in the combustion chamber causes a thermal expansion and pressure increases in this confined space. These gases are then accelerated and ejected through the nozzle. Depending on how the propellants are stored, rocket engines are categorised as liquid, solid or hybrid engines. We will focus on the first.

The thrust magnitude of such an engine is separated into two components, as shown in equation (1.1) where u_e and p_e are the velocity of the accelerated gases and the pressure at the nozzle exit, A_e is the cross-section area, p_∞ is the ambient pressure and $\dot{m}$ is the mass flow rate. The first term is the impulse thrust and the second is the pressure thrust. Due to the shape of the nozzle, maximum thrust is obtained if $p_e = p_\infty$ [7].

$$F = \dot{m}u_e + A_e(p_e - p_\infty) \quad (1.1)$$

With the high costs of launching cargo into space, the main concern is to keep the weight as low as possible while still having enough thrust to propel the vehicle. The specific impulse, I_{sp}, is the ratio between the total impulse, I_t, and the weight of propellant as shown in equation (1.2). Here, the mass of propellant, m_p, divided by the time of combustion, t_b, yields $\dot{m}$

and by applying the condition for maximum thrust mentioned above, it becomes apparent that the specific impulse can only be increased with the velocity of the expelled gases. This parameter shows how much thrust can be obtained from a unit of weight of propellant and therefore a high I_{sp} is desirable.

$$I_{sp} = \frac{Ft_b}{m_p g_0} = \frac{u_e}{g_0} \quad (1.2)$$

By assuming a steady and isentropic flow the energy conservation equation leads to a constant value of $h + u^2/2$ where h is the enthalpy. Hence, and since $h = c_p T$, one can write

$$c_p T_e + \frac{u_e^2}{2} = c_p T_{cc} + \frac{u_{cc}^2}{2} \quad (1.3)$$

where T_{cc} and u_{cc} are the temperature and velocity in the combustion chamber.

By assuming a negligible velocity inside the chamber and rewriting the isobaric specific heat as a function of the adiabatic index γ and the ideal gas constant R, we arrive at

$$u_e = \sqrt{\frac{2\gamma}{\gamma - 1} R T_{cc} \left[1 - \frac{T_e}{T_{cc}}\right]} = \sqrt{\frac{2\gamma}{\gamma - 1} R T_{cc} \left[1 - \left(\frac{p_e}{p_{cc}}\right)^{\frac{\gamma-1}{\gamma}}\right]} \quad (1.4)$$

It becomes clear that the velocity of the gases at the exit of the nozzle increases with the chamber pressure, along with the specific impulse. This justifies the desire for higher pressures inside the combustion chamber, leading to a transition into the supercritical regime as the liquid propellants are heated when exiting the injector. The RS-25, the Vulcain and the Vinci engines are only a few examples of Liquid Rocket Engines (LREs) that operate with chamber pressures above critical conditions [8–10]. Coaxial injection of oxygen and hydrogen constitutes a typical configuration in this type of engine.

Understanding the flow dynamics under these conditions is crucial to create better and more reliable tools to simulate and optimise rocket engine performance. Researchers started by studying a simpler setup with liquid nitrogen instead of oxygen as the injected oxidiser for safety concerns and to diminish the pressure in the test facility, since the critical pressure of nitrogen is nearly two thirds that of oxygen. [11] explains that the reported results are similar as long as there are no chemical reactions. Furthermore, to avoid variation of material properties due to species mixing, the fuel can be injected into a chamber filled with gaseous nitrogen.

Experimental studies with supercritical fluids are costly and hard to execute. Additionally, despite still not being the reference when studying a certain phenomenon, when validated for a specific set of conditions, Computational Fluid Dynamics (CFD) can provide invaluable information that an experimental study cannot. The validation of a numerical setup under these simplified conditions (LN_2/GN_2) can therefore be seen as a first effort towards accurately and reliably simulating combustion phenomena inside an LRE combustion chamber.

1.1 Objectives

A small step in the direction of the validation of the numerical setup discussed in the previous section is to understand how current turbulence models, calibrated for subcritical conditions, behave under supercritical conditions. With an accurate thermodynamic formulation, we evaluate the efficiency and accuracy of each tested model and try to link the structure of each one or the presence of specific terms to certain characteristics of the final results. This comprises one of the objectives of this study.

Additionally, by comparing the obtained results to those of other researchers, we aim to cement the conviction that simple turbulence models can in fact produce very accurate results at a much reduced computational cost, when compared to Large Eddy Simulation (LES).

Finally, we seek to provide some insight into the error induced by the most commonly used Equations of State (EoS) under these conditions. With this in mind, two cubic EoS are compared to a reference EoS for nitrogen, used as a benchmark.

By working towards understanding the phenomena inside an LRE combustion chamber, we hope this study will help the industry find its way in adopting more cost efficient yet still reliable design process tools.

1.2 Overview

The present work is divided into a series of chapters: Introduction, Theoretical Review, Mathematical Model, Implementation, Results and Discussion and finally Conclusions and Future Work. In the second chapter, an updated review of the scientific research made until this point is presented in terms of supercritical phenomena next to relevant experimental and numerical studies. Chapter three focuses on describing the equations and considerations applied to define the flow dynamics and thermodynamics, moving on to chapter four that goes on describing the methodology used to apply said equations to a discrete domain with the least possible amount of numerical error. In chapter five, the results obtained with the described mathematical model are validated against experimental data as well as against other numerical data. Finally, in chapter six, conclusions are drawn from the current investigation and, with the groundwork laid, suggestions for future work are presented.

Chapter 2

Theoretical Review

This chapter is dedicated to discussing the supercritical regime and its main implications on fluid behaviour. After this initial discussion, we move on to the relevant experimental studies and measuring techniques and finally to the respective numerical studies. But before going that far, it is helpful to introduce some basic concepts and definitions.

At an arbitrary constant temperature, a gas can be converted to a liquid by increasing the pressure. However, as the temperature increases, so does the kinetic energy of the molecules along with the pressure needed to bring the gas to a liquid. The critical temperature, T_c, marks the point after which a transition to the liquid phase is no longer possible, no matter the applied pressure. The vapour pressure at the critical temperature is then defined as the critical pressure, p_c. The critical point then marks the end of vapour pressure line, where both temperature and pressure reach their critical values. Here, physical properties change dramatically and become identical for the liquid and gas phases, the isobaric specific heat is infinite while both surface tension and latent heat are zero, though this will still be discussed in section 2.1. The position of this point is affected by the magnitude of the intermolecular attraction forces meaning that it is specific to each substance. Nitrogen is the subject of this study and Table 2.1 can be used to locate its critical point in a phase diagram.

On a final note, several authors divide the supercritical regime into different regions which we briefly mention in the upcoming section. However, following the work from [12], we define supercritical as the region of $T > T_c$ or $p > p_c$ in which there is no phase equilibrium and therefore no phase transition. Despite the absence of a phase transition, we will still discuss how properties can be severely altered inside the supercritical regime through non-equilibrium processes.

Table 2.1: Critical properties of nitrogen

Properties	Value
T_c [K]	126.192
ρ_c [$\mathrm{kg \cdot m^{-3}}$]	313.30
p_c [MPa]	3.3958

2.1 Considerations on the supercritical regime

When dealing with supercritical fluids, the borders in a phase diagram are an interesting point of discussion. One can imagine a diagram as that of Figure 2.1 where the critical temperature and pressure create three additional regions besides the subcritical gaseous and liquid phases. We mention this diagram only as a stepping stone to introduce a modified diagram that considers a different border and that is of bigger interest in this study.

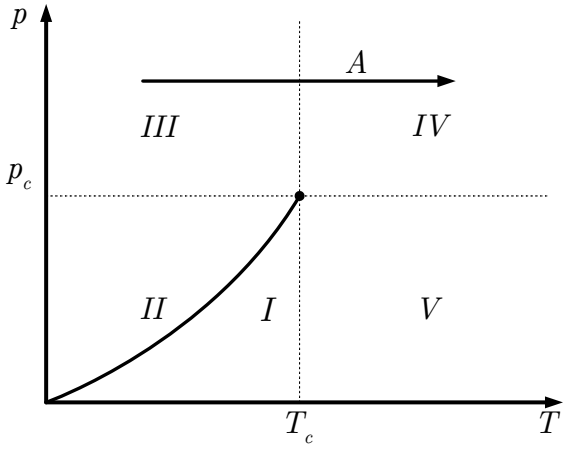

Figure 2.1: Fluid phase diagram [13]

By comparing the molecular arrangement in a liquid, in region II, to that of a supercritical fluid, in region III, [13] shows that the molecular disposition in both cases bares no differences. When moving through A, however, the substance switches from liquid-like to gas-like fluid at some point in region IV. Data obtained from the NIST database presented in Figure 2.2 clearly shows that the supercritical regime can indeed harbour fluids of different characteristics and with different density values. While different isobaric lines converge to different density values for higher temperatures, they arrive at generally the same value of density for lower temperatures indicating once more a liquid-like incompressible behaviour.

This transition from a liquid-like to a gas-like fluid could be compared to a subcritical boiling, the main difference being that the isothermal vaporisation typical of subcritical fluids is replaced by a continuous non-equilibrium process that takes place over a finite temperature range. As this happens, the specific heat capacity goes through a maximum and actually tends to infinity when approaching the critical point, as shown in Figure 2.2. Much like [11], we refer to this transition phenomenon as pseudo-boiling and to the maxima of specific heat capacity as pseudo-boiling line.

With this, [14] presents an altered phase diagram, shown in Figure 2.3, where the pseudo-boiling line is a direct continuation of the subcritical vapour pressure line. The effects of crossing the pseudo-boiling line play an important role in the present study so we shall use this diagram as a reference.

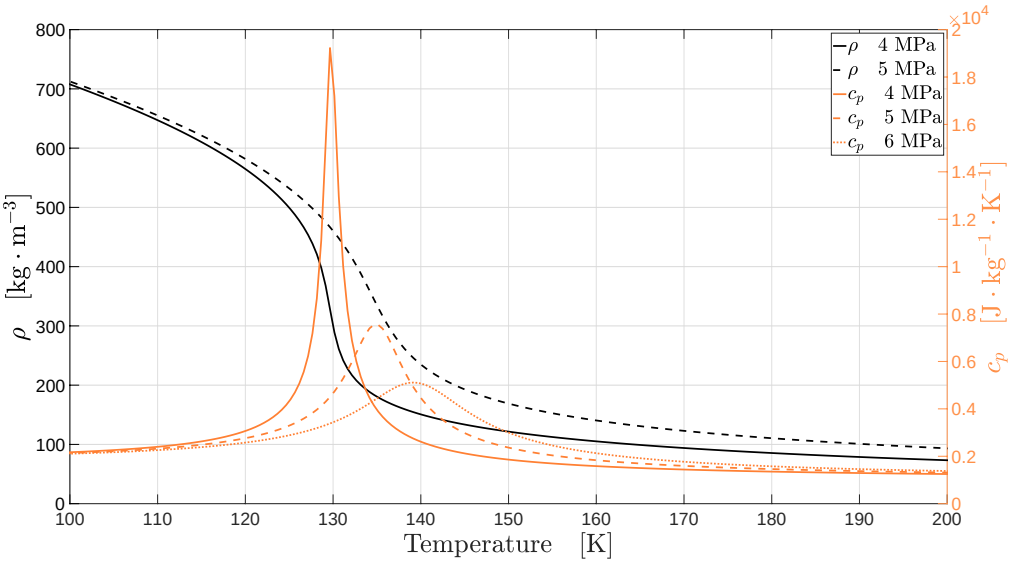

Figure 2.2: Density and isobaric specific heat values for nitrogen (data from the NIST database)

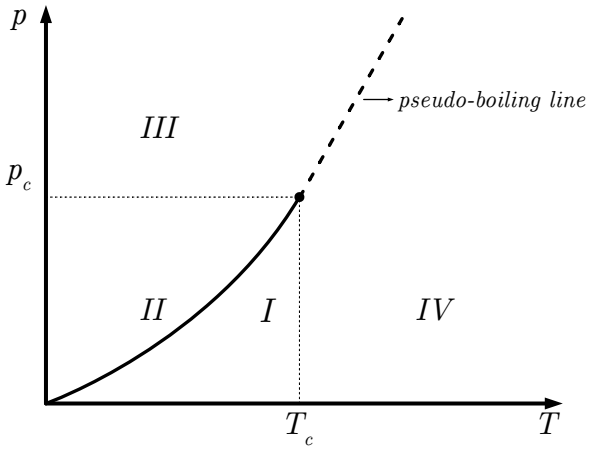

Figure 2.3: Adopted phase diagram [14]

Besides the specific heat, the molecular viscosity and the thermal conductivity are also greatly affected during this transition as shown in Figure 2.4. For these two properties, as well as for the specific heat, it is clear that a static value cannot be used since it would produce largely unrealistic results. Sections 3.5 and 3.6 are dedicated to properly defining these quantities.

Density prediction must also be minded. We have already observed the strong density gradients in Figure 2.2 where, for $p = 4\,\mathrm{MPa}$, a $1\,\mathrm{K}$ increase at $129\,\mathrm{K}$ is responsible for a 21% reduction in density values. With this kind of behaviour, a constant density value cannot be set and [15] shows that even the ideal gas equation proves very unreliable in this region. To solve this problem, a series of real gas EoS can be applied to their specific advantages and disadvantages.

Multi-parameter EoS can produce very accurate results but are immensely consuming in

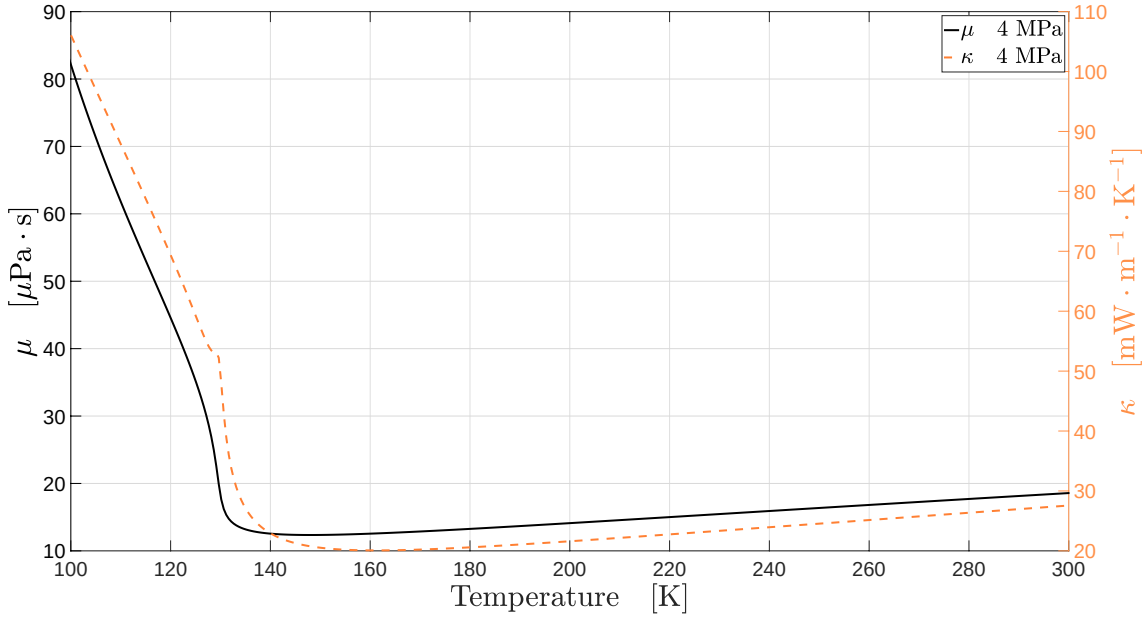

Figure 2.4: Viscosity and thermal conductivity values for nitrogen (data from the NIST database)

terms of computational power. Such equations can be created through polynomial and exponential expansions where the coefficients multiplied by each term are specific to each fluid. These coefficients must be fitted through the available experimental data for the conditions in which the EoS is to be valid. The 32-term modified Benedict-Webb-Rubin (MBWR) [16] EoS achieves a relative density error smaller than 0.5% above and below the critical point. [17] proposes a 12-term EoS with available coefficients for a series of substances, nitrogen included, while [18, 19] provide a highly accurate 18-term EoS optimised directly for nitrogen with a relative density error no higher than 0.042% for the test conditions used in this work, listed in Table 4.1. The major drawback with this approach is the CPU cost and, in most cases, this factor alone prohibits the use of multi-parameter EoS.

An alternative is to use a multi-parameter EoS to calculate fluid properties prior to the numerical simulation start and store these values in a library to be accessed during runtime, thus completely eliminating the need for any further calculations. The initial computational cost necessary to create this library for a wide range of temperature and pressure with sufficient resolution is elevated but the profit is high since this only has to be done once. This method is extremely captivating due to the obvious accuracy gain over simpler EoS and simultaneous computational cost reduction. [14] implements this type of library in his study and ANSYS® also allows for the usage of a real-gas library [20] as discussed in section 3.4.

Both the Soave-Redlich-Kwong (SRK) EoS [21] and the Peng-Robinson (PR) EoS [22] are widely used for their simplicity since they only employ three parameters specific to each species, related to intermolecular forces and the finite volume of each molecule. Both of these EoS have been used by a series of researchers in other studies, as shall be discussed in section 2.3. Nevertheless, their accuracy and the dependent variables must be monitored

and considered when evaluating simulation results. [23] reports a noticeable error for these two equations in the critical region when compared to the multi-parameter Benedict-Webb-Rubin (BWR) EoS [24]. Here, the relative density error for the SRK and PR EoS goes up to 13% and 17% respectively, at approximately $10\,\mathrm{MPa}$. These errors are not for nitrogen but oxygen instead and at a very high reduced pressure so they serve only as a warning. The influence of the different EoS in the present study cases is presented and discussed in section 5.1.1 where the results obtained using these two cubic EoS are compared to those when using the REPROPv9.1.

On another matter, we know that in a subcritical injection surface instabilities are responsible for jet atomisation where small discrete ligaments begin to break up and droplets are ejected from the jet core as can be seen in Figure 2.5a. In a supercritical injection, however, the breakup mechanics are entirely different. [25] describes one of the main characteristics of supercritical fluids as the impossibility of a two-phase flow due to the disappearance of the surface tension at and beyond the critical point. Similar effects are reported by [11] where the surface tension is measured for oxygen from subcritical temperatures, with higher values, up to the critical temperature, for which it completely vanishes.

Several other authors describe this different breakup mechanism where the drops and ligaments are no longer detected and no distinct surface interface can be determined. [25] notes that this disintegration mechanism more closely resembles turbulent and diffusive mixing than the traditional jet disintegration and [14] describes a thermal-breakup mechanism where the limit of the jet core is defined by the transition of the fluid across the pseudo-boiling line. Figure 2.5b clearly shows how the interface dissolves between the two fluids.

The Knudsen number (Kn) describes the degree of departure from continuum and is defined as the ratio between the mean free path, average distance travelled by a molecule between collisions, and the characteristic length of the problem. If the Kn number is low enough, momentum transfer and collision between molecules is predominant but, for higher values, molecules become increasingly more independent of one another and the equations used to define fluid dynamics become invalid. [6] makes use of this measurement to describe the interface dissolution in the supercritical regime. The author studies this phenomenon for fuel inside the combustion chamber of diesel engines and comes to the conclusion that in a supercritical regime, the interface thickness between the two fluids greatly increases along with a reduction in surface tension. At the interface, in subcritical conditions, the Knudsen number (Kn) is well above 0.1 and a continuum flow cannot be considered across this interface so a discrete two-phase method has to be implemented in numerical simulations. For a supercritical injection, on the other hand, the increase in interface thickness lowers the Kn number and creates an acceptable continuum flow regime. This means that the governing equations apply across this interface thus validating the usage of a single phase flow approach.

In the end, both the thermodynamic behaviour and the breakup mechanisms have a direct effect on the jet structure. As the liquid-like nitrogen is injected into the chamber, its tem-

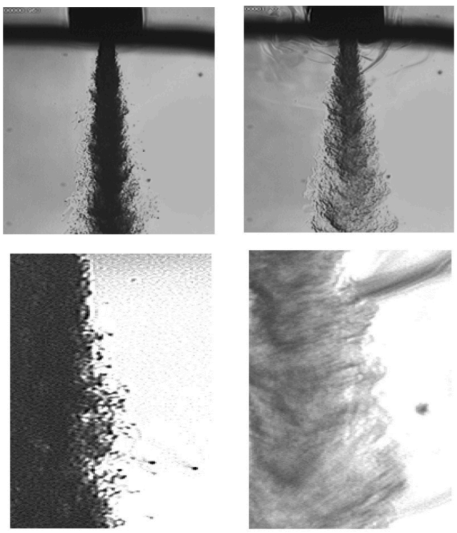

(a) $p/p_c = 0.91$ (b) $p/p_c = 2.71$

Figure 2.5: Liquid nitrogen injected into a heated nitrogen environment at sub- and supercritical pressures [26]

perature increases as it begins to mix with warmer gas-like nitrogen. The structure of the flow changes and it can be divided into three characteristic regions as Figure 2.6 shows. [27] defines the length of the potential core as the distance at which the centreline density remains relatively constant and [14] compiles and compares four different equations attempting to predict this length that are either based on the ratio between the densities of the liquid and gas-like fluids or are given a constant value for any specific test geometry. In the self-similar region, the absolute value of flow variables can still change but their radial profiles are no longer a function of axial direction. In between these two regions is the transition zone where the turbulent and diffuse mixing are most relevant. As instabilities begin to appear, dense pockets of liquid-like nitrogen are separated from the jet core causing an increase in density fluctuations [28, 29]. As a result, density sharply decreases and energy dissipation is significative.

In experimental studies, this structure is visible through the axial and radial density distributions and also through the jet spreading angle. These measurements are then used by the numerical studies for validation of the results, discussed in sections 2.2.3 and 2.3.

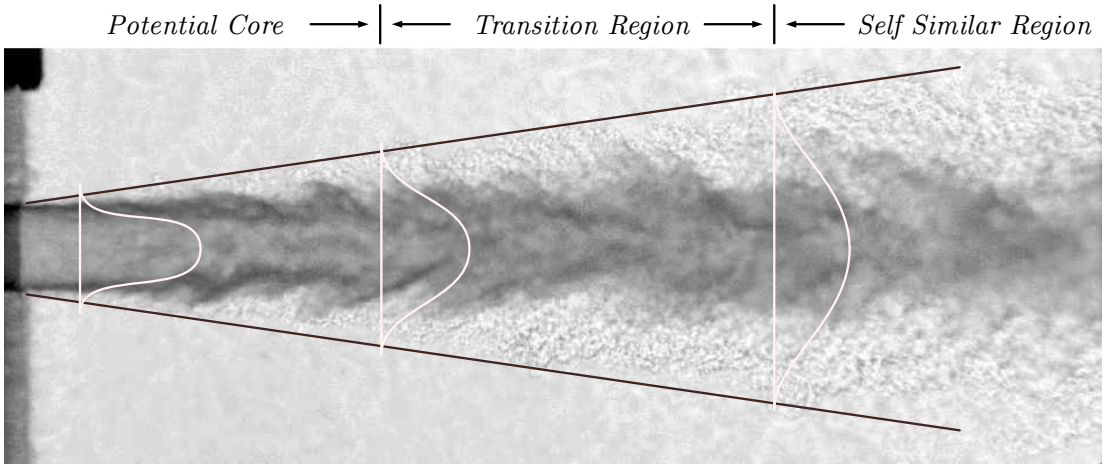

Figure 2.6: Jet mixing flow field [27]

2.2 Experimental work

After a small introduction of the behaviour of a supercritical fluid, it seems appropriate to discuss how it can be experimentally studied and measured. For the time being, Computational Fluid Dynamics (CFD) tools need to be validated by experimental results due to the lack of a general, efficient and accurate mathematical formulation. But experimental studies are not deprived of error and uncertainty whether from the user, the equipment or the measuring techniques. Even more so, in the present case of supercritical fluids where the desired test conditions are hard to maintain while measuring and visualisation techniques become more restricted, such errors can have a strong impact on the outcome. It is therefore very important, when using CFD tools to study a certain phenomenon, to be familiarised with its experimental counterpart to allow for an informed critical analysis during the validation process. The experimental studies here discussed make use of two main measuring techniques: Shadowgraphy and Raman spectroscopy. Sections 2.2.1 and 2.2.2 are dedicated to the discussion of each of these measurement techniques and section 2.2.3 to the relevant experimental studies and their findings.

2.2.1 Shadowgraphy

Shadowgraphy is a powerful tool that allows to qualitatively study the dynamics of fluids through flow visualisation. The basic structure of this setup is presented in Figure 2.7 where the light beam is initially redirected before reaching the test facility. After it crosses the fluid, it is once again adjusted, as shown in Figure 2.8, before arriving at a film that is sensitive to the light intensity. As described by [30], this light intensity and the captured contrast are dependent on the second derivate of the density meaning that in Figure 2.5b, even if a certain area retains a certain shade of grey, the density can be changing. What remains constant is its rate of change.

Unlike the technique described in the next section, this is a non-evasive method meaning that it does not alter the composition or behaviour of the test subject. As discussed, it can

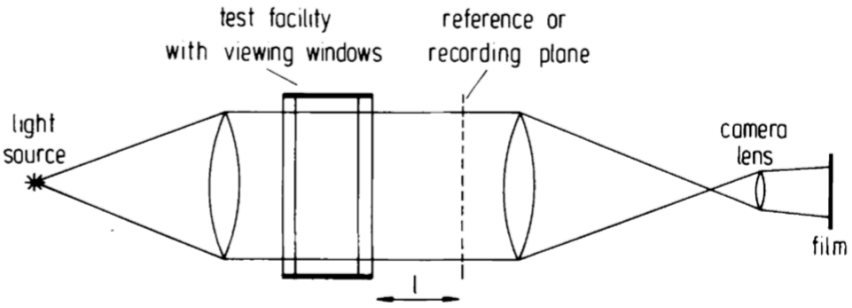

Figure 2.7: Shadowgraph instalation [30]

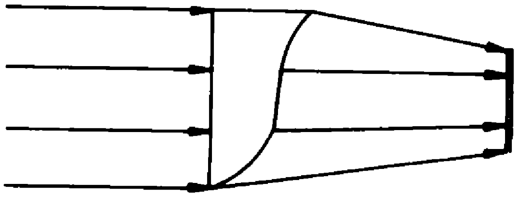

Figure 2.8: Deflection of light rays on a variable second density environment [30]

be used to study the structure of the jet, but it is not suitable to quantify the density field that is being observed. To solve this problem, shadowgraphy can be combined with Raman spectroscopy.

2.2.2 Raman spectroscopy

When radiation impacts on a certain substance, light is scattered in different directions with the same wavelength as the incident beam. Such elastic collisions where the energy of the impacting photon remains unchanged are referred to as Rayleigh scattering. [31] discovered in 1928 that additional diffuse radiation is also present with an altered wavelength. This wavelength shift represents the energy that is absorbed or emitted by molecules. The resulting frequency is dependent on the molecular structure meaning that it can be used to identify the substance in question. Additionally, the Raman signal intensity, I, is proportional to the number density and to the scattering cross-section, amongst other parameters. [32] explains that by considering a constant cross-section, the density values can be calculated as shown in equation (2.1). However, the author warns that this assumption can lead to an underestimation of the density values in the cases where an initial dense potential core is present.

$$\rho = \frac{I}{I_\infty}\rho_\infty \quad (2.1)$$

The scattered radiation is regrettably small and a strong light source is needed. While Raman initially used sunlight as a source, present day researchers make use of monochromatic laser beams. By lowering the wavelength, the scattered radiation is increased and better results can be obtained, but this comes at the cost of possible photo-decomposition and spikes in density values.

[27, 32] mention additional challenges in high density regions that reduce the amount of scattered radiation. This happens because of the high refraction index that redirects some of the signal along the jet axis. As a result, the measured density in this region can be somewhat underestimated. In one of the test cases of [27], the maximum measured density is of $400\,\mathrm{kg/m^3}$, but for the reported injection temperature of $126.9\,\mathrm{K}$, the corresponding density value is of $457.82\,\mathrm{kg/m^3}$, accounting for a relative density error of 12.6%. While this is a major source of error along the potential core, it has little influence further downstream where the density starts to decrease along with the refraction effects. When analysing the results, it is important to remember that an overestimation of the density values in the potential core when compared to the experimental results is expected and that both should begin to coincide in the transition region.

2.2.3 Study cases

There are a series of experimental studies on supercritical injection, but we shall focus the discussion on those that deal only with nitrogen. In the work produced by [32] the injection temperature varies between sub- and supercritical values but always at supercritical pressures. With this, the axial distributions of density and temperature are studied and compared for two different chamber pressure conditions. The shape of the density and temperature radial profiles are also published to analyse the transition from an initial top hat shape to a free jet profile typical of a self-similar region. This is complemented by the Full Width Half Maximum (FWHM) measurements taken from the temperature and density profiles that have not only different rates of growth but also different magnitudes.

While the aforementioned author studies both the temperature and density profiles, [33] focuses on the latter. In his setup, Raman scattering is used to measure the structure of a nitrogen jet at sub- and supercritical pressures. Some of the most interesting conclusions of this work are related to the measuring techniques themselves but insight is also given in regards to the supercritical regime. The author plots the density along the radial direction to study the differences between the density profiles for $p/p_c = 0.43$ and $p/p_c = 2.03$. He then compares these density profiles for different axial positions to identify a self-similar region in the jets. Some emphasis is also put into studying the jet spreading angle and growth rate. While several methods are discussed, the FWHM measurement of density is regarded as the most appropriate choice when multiplied by a factor of 2 for supercritical pressures. With these measures, the author reports an increase in the jet growth rate with increasing pressure. Similar observations are made in [26] where there is an added interest in studying the nature of the jet. By analysing the disintegration process and the mixing layer both qualitatively (through Shadowgraphy) and quantitatively (through Raman spectroscopy), similarities appear between supercritical and variable density incompressible gaseous jets, justifying the need for the Favre averaging method.

In the experimental setup of [34], pressures are kept at supercritical values and the influ-

ence of the injection temperature and velocity is studied. Raman spectroscopy is once again applied to measure the density values that are then plotted along the axial and radial directions, in addition to velocity and temperature profiles. With this, the author is capable of analysing the structure of the jet and the influence of each parameter and concludes that the temperature has a stronger influence than the pressure and velocity in the flow field. The author mentions the absence of a potential core in some test cases when compared to the numerical results and justifies this with the quality of the Raman images and a possible heating mechanism inside the injector. Nevertheless, potential core lengths are compared to two different relations, one of which provided in [33]. The spreading angle calculated through the $2\times$FHWM is compared to the spreading angle calculated through the shadowgraph images and numerical results, showing discrepancies for some cases. The work produced by [34] is later followed by [27, 35] where additional experimental data are published and analysed, and correlations are offered for the potential core length and for the jet spreading angle.

Finally, both [26, 34] discuss the effects of buoyancy and arrive at the conclusion that in the region of $0 < \mathrm{x/d} < 30$, these effects can be neglected in favour of the inertial forces.

2.3 Numerical work

The three studies [27, 34, 35] performed at the DLR provide valuable and extensive information regarding not only the experimental process and data but also the numerical counterpart. Additionally, they are used to validate a considerable amount of numerical studies. To have as much data for comparison as possible, we have chosen to replicate these test conditions. Yet, some numerical studies have recurred to other test conditions and while this excludes their results from direct comparison with ours, it still allows for a qualitative analysis since the phenomenon remains largely similar.

When looking at the numerical studies in these conditions, we see a clear preference for cubic EoS. [15, 28, 29, 36–43] have selected some form of the PR EoS to define the evolution of density in the critical region. [28, 29, 40–43] added a correction to the PR EoS to considerably reduce the error in the critical region while [15, 39, 44, 45] have used the SRK EoS. For his numerical calculations, [35] reports the use of the MBWR model and two authors, [14, 46], have gone further by using a real gas library. Transport properties have also been defined in a more accurate manner, with the trend being the definitions provided by [47].

The modelling of turbulence is still one of the most important topics of discussion. With the advent of CFD, the available range of fidelity has increased in regards to new turbulence models, LES and Direct Numerical Simulation (DNS). Recently, [28, 29] performed a three-dimensional DNS for conditions similar to those of case 3 but with a lower Reynolds (Re) number to allow for a coarser mesh. Except for the shorter potential core caused by the lower Re number, results for the axial density decay are in excellent agreement with the experimental measurements, which is to be expected from DNS. But this method is, for now,

very restrictive and the interest has been mainly in LES. The results from [36,37] are indeed quite accurate for case 3 but, for some reason, the density values are largely underestimated for case 4 where an unrealistic potential core is also observed.

The cooperative work from [41–43] between two universities compares results from a pressure and a density based solver. Both of which show results that agree with each other but that do not agree with the ones from [36]. In this case, the density values in the transition region are slightly over estimated for case 3 and, while they do agree fairly well with the experimental data for case 4, there is once again an unrealistic potential core. Similar results are obtained by [40] for both case 3 and 4. Another LES simulation by [48] can provide acceptable results for case 3, depending on the chosen parameters, but here the density values for case 4 are under estimated in the transition region with yet another unrealistic potential core. The results based on some variation of the PR EoS from the previously described simulations are displayed in Figure 2.9 for a clear overview of how they differ so strongly from one another. We present them in a non-dimensional form through ρ^+, defined in equation (2.2), where ρ_0 is the injection density and ρ_∞ is the farfield density. Both the injection and farfield density values are obtained from the NIST database [49] for the respective pressure and temperature values. Still in this figure, $\mathrm{x/d}$ is the axial coordinate normalised by the injector diameter. It is clear that all results show different behaviours in case 4, but have a common potential core that does not agree with the experimental data.

$$\rho^+ = \frac{\rho - \rho_\infty}{\rho_0 - \rho_\infty} \quad (2.2)$$

To assess the need for such costly methods, [15] compares results obtained from LES simulations with those from four different $k-\varepsilon$ based turbulence models, including [50,51]. The author concludes that, with the correct variation, the results closely match those from the LES simulations. He also notes the influence of different EoS leaving the question if the results discussed so far differ mainly due to the LES parameters or due to the thermodynamic modelling.

Ultimately, [27, 39, 52] study this phenomenon solely through turbulence modelling. The three have implemented a $k-\varepsilon$ based model and there is a fairly good agreement with experimental data for both case 3 and 4, except for the potential core predicted in case 4. In [39] the axial density decay does not seem to match for case 4, but it is worth noting that the dimensional data, reconstructed from the normalised density values, does not match that of other authors indicating an error in the reconstruction process. This observation seems to be supported by the comparison made in [44].

By looking at the studies already discussed, it is clear that the trend is either LES or a $k-\varepsilon$ based model. To the knowledge of the author, only two works have expanded their study in this field. Coupled with a pre-calculated real gas library, [14] uses the Spalart-Almaras [53] model and [46] studies how different turbulence models behave under supercritical conditions. The results show that there are indeed differences between each one, but the general

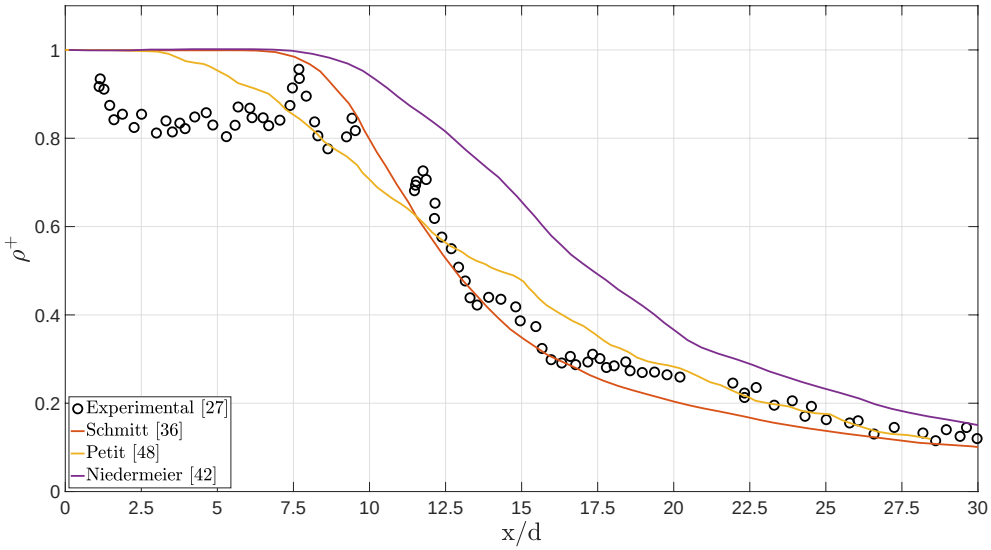

(a) Case 3

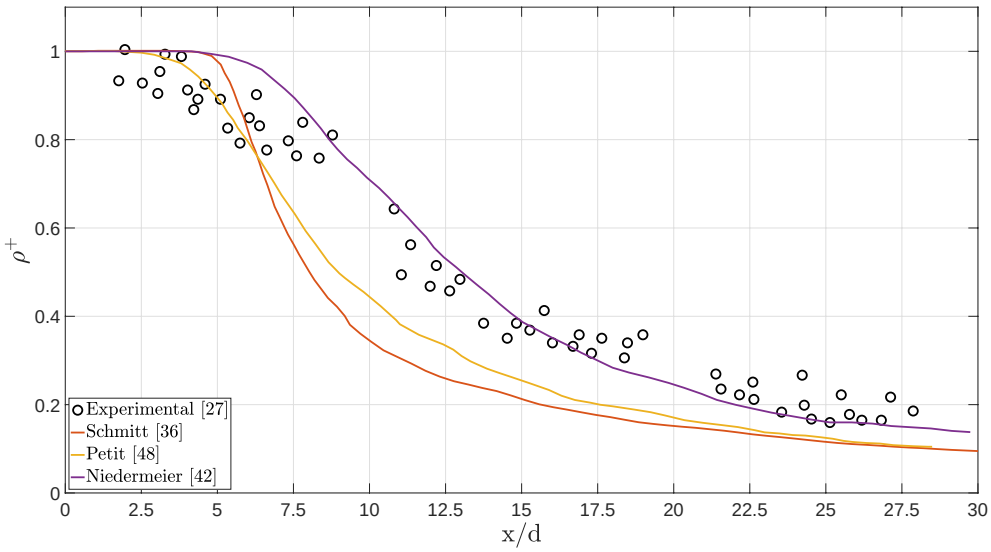

(b) Case 4

Figure 2.9: Comparison of LES simulations [27, 36, 42, 48]

trend reasonably follows the experimental data.

Despite the stark interest in LES over the past years, results vary by a large margin and are, at best, comparable to those obtained through simpler formulations. Figure 2.10 gives a clear and undoubtedly strong impression that there is no direct correlation between the complexity of a turbulence model and the quality of the results.

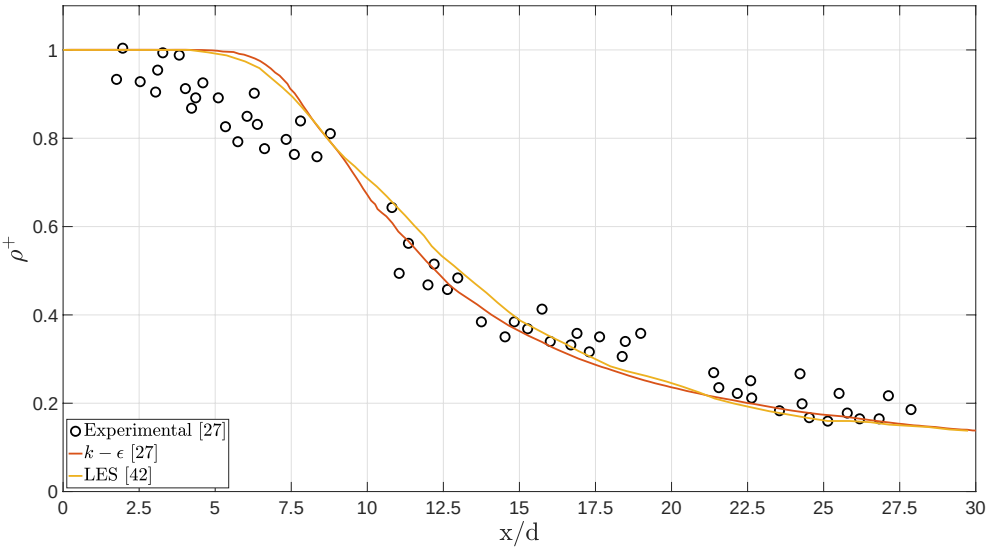

Figure 2.10: Comparison between $k-\varepsilon$ model and LES [27, 42]

2.4 Summary

So far, we have had the chance to introduce the supercritical regime along with its influence on the physical properties of nitrogen. By crossing the pseudo-boiling line, the specific heat capacity momentarily increases to a maximum and the density values change dramatically along with the molecular viscosity and thermal conductivity. Several methods can be adopted to accurately predict the values of these properties in this region, each with their specific advantages and complexity. Additionally, the disappearance of surface tension in the supercritical regime leads to an altered jet structure that more closely resembles the injection of a gaseous turbulent jet into a gaseous environment. This structure has been studied both experimentally and numerically. While in experimental cases it is important to be familiar with the process and to be aware of measurement error sources, in numerical studies it is interesting to compare the outcome of different turbulence prediction methods. The research available thus far is mainly concentrated on LES or $k-\varepsilon$ turbulence models and comparison studies on this subject are scarce. Having reached this far, we can now introduce a mathematical model appropriate to the test conditions.

Chapter 3

Mathematical Model

This chapter is sectioned into different fields. One must start with the concept of a conservation law and the equations that define the transport of a set of conserved quantities. Afterwards, approximations to specific terms in these equations have to be made to simplify their resolution. Turbulence modelling is one of the major aspects in this field but there are other factors to be considered such as the modelling of thermodynamic properties. The mathematical model is implemented through the software ANSYS® FLUENT®, and while most of the desired settings are readily available, some have to be applied through User Defined Functions (UDFs). Also important is to remember that some turbulence models here introduced are not directly taken from the original source but instead adjusted by ANSYS®, making the solver manual, [20], the recommended source of information.

3.1 General form of a conservation law

The concept of conservation law is here introduced and applied to mass, momentum and energy per unit volume. If we consider the surface S delimiting the volume Θ, the variation in time of the scalar ϕ inside that same volume is

$$\frac{\partial}{\partial t}\int_{\Theta}\phi \mathrm{d}\Theta \quad (3.1)$$

and the flux is a vectorial quantity normal to S defined by the rate at which ϕ crosses this surface so that

$$-\oint_{S} F_i \mathrm{d}S_i \quad (3.2)$$

A flux can be divided into two categories. An advective flux is characterised by the passive transport of ϕ by the bulk of the fluid. A diffusive flux, on the other hand, is proportional to the concentration of ϕ across the domain, i.e., the higher the gradient of ϕ the higher its diffusive flux. The advective flux is defined as

$$F_{A_i} = \phi u_i \quad (3.3)$$

and the diffusive flux as

$$F_{D_i} = -\Gamma \frac{\partial \phi}{\partial x} \quad (3.4)$$

where Γ is the diffusivity coefficient.

With the temporal variation and the flux contributions defined, two more terms can be added to the conservation equation of ϕ to account for surface and volume sources:

$$\int_{\Theta} Q_{V_i} \mathrm{d}\Theta + \oint_{S} Q_{S_i} \mathrm{d}S_i \quad (3.5)$$

The terms from equations (3.1) (3.2) and (3.5) represent all the possible contributions to the evolution of a conserved quantity. By summing them up and applying the Gauss theorem, the integral form of the conservation equation is obtained in equation (3.6).

$$\int_{\Theta} \frac{\partial \phi}{\partial t} \mathrm{d}\Theta + \int_{\Theta} \frac{\partial F_i}{\partial x_i} \mathrm{d}\Theta = \int_{\Theta} Q_{V_i} \mathrm{d}\Theta + \int_{\Theta} \frac{\partial Q_{S_i}}{\partial x_i} \mathrm{d}\Theta \quad (3.6)$$

Additionally, in can be expressed as

$$\int_{\Theta} \left[\frac{\partial \phi}{\partial t} + \frac{\partial}{\partial x_i} (F_i - Q_{S_i}) \right] \mathrm{d}\Theta = \int_{\Theta} Q_{V_i} \mathrm{d}\Theta \quad (3.7)$$

In equation (3.7), the flux is joined with the surface source term since they tend to have a similar behaviour. The term $(F_i - Q_{S_i})$ can therefore be considered as an effective flux.

3.1.1 Mass conservation equation

For the conservation of mass, ϕ is replaced by ρ. Mass can neither be created nor destroyed and as a result, there is no diffusive term in equation (3.8), only an advective one. In the absence of external mass sources, the mass conservation equation, also known as continuity equation, is in its integral form:

$$\int_{\Theta} \left[\frac{\partial \rho}{\partial t} + \frac{\partial}{\partial x_i} (\rho u_i) \right] \mathrm{d}\Theta = 0 \quad (3.8)$$

3.1.2 Momentum conservation equation

Momentum is a vectorial quantity meaning that its transport is defined by as many equations as the number of dimensions that are assumed. For this case, $\phi_j = \rho u_j$ and the momentum advective flux is thus defined as

$$F_{A_i} = \rho u_j u_i \quad (3.9)$$

Again, we assume the inexistence of diffusion of momentum, as we did for the continuity equation, eliminating the diffusive flux term.

External volume forces are introduced through the volume source term as ρf_i. Also, inside the control volume Θ, the internal forces cancel each other but this does not happen on the surface S for which there is no counter action. This results in the surface source term

$$Q_{S_i} = \sigma_{ij} \quad (3.10)$$

where the internal stress tensor σ_{ij} is defined by its anisotropic and isotropic components:

$$\sigma_{ij} = t_{ij} - p\delta_{ij} \quad (3.11)$$

In equation (3.11), the viscous shear stress is defined by the tensor t_{ij}. In equation (3.12) it is defined as function of both the molecular viscosity, μ, and of the second viscosity, replaced by $-2/3\mu$, leading to

$$t_{ij} = 2\mu\left(s_{ij} - \frac{1}{3}\frac{\partial u_k}{\partial x_k}\delta_{ij}\right) \quad (3.12)$$

where s_{ij} is the strain-rate tensor

$$s_{ij} = \frac{1}{2}\left(\frac{\partial u_i}{\partial x_j} + \frac{\partial u_j}{\partial x_i}\right) \quad (3.13)$$

Applying the previous terms to the structure from equation (3.6), leads to the momentum or Navier-Stokes equations in their integral form:

$$\int_\Theta \left[\frac{\partial}{\partial t}(\rho u_i) + \frac{\partial}{\partial x_j}(\rho u_j u_i)\right]\mathrm{d}\Theta = \int_\Theta \left[-\frac{\partial p}{\partial x_i} + \frac{\partial t_{ij}}{\partial x_j} + \rho f_i\right]\mathrm{d}\Theta \quad (3.14)$$

3.1.3 Energy conservation equation

The total energy of a fluid can be expressed as the sum of its internal energy, e, and its kinetic energy per unit mass:

$$E = e + \frac{u_i u_i}{2} \quad (3.15)$$

If one considers the conserved quantity $\phi = \rho E$, then the advective flux is

$$F_{A_i} = \rho E u_i \quad (3.16)$$

and the diffusive flux is, through Fourier's law of heat conduction,

$$F_{D_i} = \frac{\partial q_i}{\partial x_i} = -\kappa\frac{\partial T}{\partial x_i} \quad (3.17)$$

where T is the absolute temperature and κ is the thermal conductivity defined by

$$\kappa = \rho c_p \alpha \quad (3.18)$$

In equation (3.18), α is the thermal diffusivity that can be used to understand the physical meaning of the Prandtl (Pr) number:

$$\mathrm{Pr} = \frac{\mu c_p}{\kappa} = \frac{\nu}{\alpha} \quad (3.19)$$

Here, ν is the kinematic viscosity and the Pr number can be interpreted as the ratio between momentum and thermal diffusion.

Finally, the distinction has to be made between volume and surface sources. The volume sources represent the sum of the work done by f_i and any heat sources other than conduction, q_H. Hence, volume sources can be defined as

$$Q_{V_i} = \rho u_i f_i + q_H \quad (3.20)$$

and the surface sources as

$$Q_{S_i} = u_i \sigma_{ij} = u_i t_{ij} - u_i p \delta_{ij} \quad (3.21)$$

With this, the energy conservation equation can be written in its integral form as

$$\int_\Theta \left[\frac{\partial}{\partial t}(\rho E) + \frac{\partial}{\partial x_j}(\rho E u_j) \right] \mathrm{d}\Theta = \int_\Theta \Bigg[- \frac{\partial q_j}{\partial x_j} + \frac{\partial}{\partial x_j}(u_i t_{ij}) - \frac{\partial}{\partial x_j}(u_i p) + \\ + \rho u_i f_i + q_H \Bigg] \mathrm{d}\Theta \quad (3.22)$$

or, by removing volume sources,

$$\int_\Theta \left[\frac{\partial}{\partial t}(\rho E) + \frac{\partial}{\partial x_j}(\rho H u_j) \right] \mathrm{d}\Theta = \int_\Theta \left[- \frac{\partial q_j}{\partial x_j} + \frac{\partial}{\partial x_j}(u_i t_{ij}) \right] \mathrm{d}\Theta \quad (3.23)$$

For the future, it is be helpful to keep in mind that the total enthalpy is defined by

$$H = e + \frac{p}{\rho} + \frac{u_i u_i}{2} = h + \frac{u_i u_i}{2} = E + \frac{p}{\rho} \quad (3.24)$$

3.2 Approximations

The conservation equations derived in sections 3.1.1, 3.1.2 and 3.1.3 cannot be directly discretised and a statistical approach must be implemented. Turbulence consists of random fluctuations of the various flow properties and in 1895 Osborne Reynolds proposed the separation of such quantities into a mean and a fluctuating part. According to this method, a time average is applied to the governing equations. However, the new fluctuating terms introduce a closure problem where the number of unknowns is higher than the number of transport equations. Turbulence modelling deals with this closure problem by introducing new transport equations to reproduce the behaviour of the fluctuating terms.

The Reynolds averaged equations are introduced for a short explanation of the concept after which the Favre averaged equations, adequate for variable density flows, are presented. Finally, the relevant turbulence modelling variants can be introduced.

3.2.1 Reynolds averaging

The backbone of the Reynolds averaging approach is the splitting a quantity into a mean and a fluctuating component

$$\phi_i = \overline{\phi}_i + \phi_i' \quad (3.25)$$

where

$$\overline{\phi}_i = \lim_{t\to\infty} \frac{1}{\Delta t} \int_t^{t+\Delta t} \phi_i \mathrm{d}t \quad (3.26)$$

$$(3.27)$$

meaning that

$$\overline{\phi_i'} = \lim_{t\to\infty} \frac{1}{\Delta t} \int_t^{t+\Delta t} (\phi_i - \overline{\phi}_i)\mathrm{d}t = 0 \quad (3.28)$$

Additionally

$$\overline{\frac{\partial \phi_i}{\partial x_j}} = \lim_{t\to\infty} \frac{1}{\Delta t} \int_t^{t+\Delta t} \frac{\partial \phi_i}{\partial x_j}\mathrm{d}t = \frac{\partial}{\partial x_j}\left[\lim_{t\to\infty} \frac{1}{\Delta t} \int_t^{t+\Delta t} \phi_i \mathrm{d}t\right] = \frac{\partial \overline{\phi_i}}{\partial x_j} \quad (3.29)$$

With equation (3.28) and equation (3.29) we can write

$$\overline{\frac{\partial \phi_i}{\partial x_j}} = \frac{\partial \overline{\phi}_i}{\partial x_j} \quad (3.30)$$

Finally, the mean of the product between a fluctuation and a mean value is zero which greatly simplifies the average of a product:

$$\overline{\phi_i \phi_j} = \overline{(\overline{\phi}_i + \phi_i')(\overline{\phi}_j + \phi_j')} = \overline{\phi}_i \overline{\phi}_j + \overline{\phi_i' \phi_j'} \quad (3.31)$$

3.2.2 Favre averaging

In order to simulate a variable density incompressible flow, the Favre averaging approach is used instead to include the effect of density variations. If one were to apply $\rho = \overline{\rho} + \rho'$ to the Reynolds averaged equations, the final formulation would be far too complex and the difficulty of establishing closure approximates would considerably increase.

The Favre averaging method eliminates this obstacle by introducing the density-weighted $\tilde{\phi}_i$:

$$\phi_i = \tilde{\phi}_i + \phi_i'' \quad (3.32)$$

where, in parallel to equation (3.27),

$$\tilde{\phi}_i = \frac{1}{\overline{\rho}} \lim_{t\to\infty} \frac{1}{\Delta t} \int_t^{t+\Delta t} (\rho \phi_i)\mathrm{d}t \quad (3.33)$$

or

$$\tilde{\phi}_i = \frac{\overline{\rho\phi_i}}{\overline{\rho}} \quad (3.34)$$

This offers a much more compact notation than that of the Reynolds averaging since $\overline{\rho\phi_i}$ can be written as in equation (3.35) instead of the Reynolds average variation in equation (3.36). While the difference may not seem enormous here, it has a much more noticeable effect when applied to the governing equations, [55].

$$\begin{aligned} \overline{\rho\phi_i} = \overline{\rho}\tilde{\phi}_i + \overline{\rho\phi_i''} = \overline{\rho}\tilde{\phi}_i \\ \overline{\rho\phi_i''} = 0 \end{aligned} \quad (3.35)$$

$$\overline{\rho\phi_i} = \overline{\rho}\overline{\phi}_i + \overline{\rho'\phi_i'} \quad (3.36)$$

And, similarly to equation (3.31), the present approach gives

$$\overline{\phi_i\phi_j} = \overline{(\tilde{\phi}_i + \phi_i'')(\tilde{\phi}_j + \phi_j'')} = \tilde{\phi}_i\tilde{\phi}_j + \overline{\phi_i''\phi_j''} \quad (3.37)$$

The concept is then applied to equations (3.8), (3.14) and (3.23) leading to

$$\int_\Theta \left[\frac{\partial \overline{\rho}}{\partial t} + \frac{\partial}{\partial x_i}(\overline{\rho}\tilde{u}_i)\right] \mathrm{d}\Theta = 0 \quad (3.38)$$

$$\int_\Theta \left[\frac{\partial}{\partial t}(\overline{\rho}\tilde{u}_i) + \frac{\partial}{\partial x_j}(\overline{\rho}\tilde{u}_i\tilde{u}_j)\right] \mathrm{d}\Theta = \int_\Theta \left[- \frac{\partial \overline{p}}{\partial x_i} + \frac{\partial}{\partial x_j}\left(\tilde{t}_{ij} + \tau_{ij}\right) + \overline{\rho} f_i\right] \mathrm{d}\Theta \quad (3.39)$$

$$\begin{aligned} \int_\Theta \left[\frac{\partial}{\partial t}(\overline{\rho}\tilde{E}) + \frac{\partial}{\partial x_j}(\overline{\rho}\tilde{u}_j\tilde{H})\right] \mathrm{d}\Theta = \int_\Theta \left[\frac{\partial}{\partial x_j}\left[- q_j - q_{t_j} + \tilde{u}_i\left(\tilde{t}_{ij} + \tau_{ij}\right) + \overline{t_{ji}u_i''} - \right.\right. \\ \left.\left. - \overline{\tfrac{1}{2}\rho u_i'' u_i'' u_j''}\right]\right] \mathrm{d}\Theta \end{aligned} \quad (3.40)$$

In equation (3.39) the instant pressure, p, is replaced by the average pressure, $\overline{p}$, and the viscous stress tensor from equation (3.12) is averaged to

$$\tilde{t}_{ij} = 2\mu\left(\tilde{S}_{ij} - \frac{1}{3}\tilde{S}_{kk}\delta_{ij}\right) \quad (3.41)$$

where the mean strain-rate tensor $\tilde{S}_{ij}$ is

$$\tilde{S}_{ij} = \frac{1}{2}\left(\frac{\partial \tilde{u}_i}{\partial x_j} + \frac{\partial \tilde{u}_j}{\partial x_i}\right) \quad (3.42)$$

The second last term in equation (3.39) is referred to as the Reynolds stress tensor and holds

correlations originated from the averaging process:

$$\tau_{ij} = -\overline{\rho u_i'' u_j''} \quad (3.43)$$

Additional terms also appear in equation (3.40) such as $\tilde{E}$, $\tilde{H}$ and the turbulent heat flux, q_{t_j}, defined by

$$\tilde{E} = \tilde{e} + \frac{1}{2}\tilde{u}_i\tilde{u}_i + k, \quad \tilde{H} = \tilde{h} + \frac{1}{2}\tilde{u}_i\tilde{u}_i + k \quad (3.44)$$

$$q_{t_j} = \overline{\rho u_j'' h''} \quad (3.45)$$

with k as the turbulent kinetic energy per unit mass:

$$\overline{\rho} k = \frac{1}{2}\overline{\rho u_i'' u_i''} \quad (3.46)$$

The double and triple correlations from equations (3.39) and (3.40) are also a product of the averaging process which is too extensive to describe here. The Reynolds stress tensor alone introduces three additional independent variables to the previous four equation system meaning that the system is not yet closed. This emphasises the closure problem mentioned earlier. A transport equation for τ_{ij} can be provided but the number of unknowns only increases and the system remains open. Nevertheless this is the essence of second-order turbulence models and it is discussed in section 3.3.7. For now, an approximation for τ_{ij} is needed.

3.2.3 Closure approximations

The terms τ_{ij}, q_j, q_{t_j}, $\overline{t_{ji} u_i''}$ from equations (3.39) and (3.40) still need to be defined. The Boussinesq approximation can be used to define the Reynolds stress tensor and is on the basis of turbulence modelling. This approximation relates τ_{ij} with the viscous stress tensor by introducing the concept of eddy or turbulent viscosity, μ_t. It is based on an analogy between the influence of the molecular viscosity on the molecular transport of momentum (at a microscopic scale) and the influence of a turbulent viscosity on the transfer of momentum caused by turbulent fluctuations (at a macroscopic scale). As a result, equation (3.41) becomes

$$\tau_{ij} \approx 2\mu_t \left(\tilde{S}_{ij} - \frac{1}{3}\tilde{S}_{kk}\delta_{ij} \right) - \frac{2}{3}\overline{\rho} k \delta_{ij} \quad (3.47)$$

and is referred to as the Boussinesq approximation. While the terms for $i \neq j$ are in fact modelled through μ_t, the trace of τ_{ij} is still exactly defined through the specific turbulent kinetic energy from equation (3.46) like

$$\tau_{ii} = -\overline{\rho u_i'' u_i''} = -2\overline{\rho} k \quad (3.48)$$

With this relation, turbulence models can focus on calculating μ_t and k.

The laminar and turbulent heat transport terms, q_j and q_{t_j}, are defined according to Fourier's law from equation (3.17) so that

$$q_j = -\frac{c_p \mu}{\mathrm{Pr}} \frac{\partial \tilde{T}}{\partial x_j} = -\frac{\mu}{\mathrm{Pr}} \frac{\partial \tilde{h}}{\partial x_j}, \qquad q_{t_j} = -\frac{c_p \mu_t}{\mathrm{Pr}_t} \frac{\partial \tilde{T}}{\partial x_j} = -\frac{\mu_t}{\mathrm{Pr}_t} \frac{\partial \tilde{h}}{\partial x_j} \tag{3.49}$$

Pr_t represents the turbulent Pr number, i.e., $\mathrm{Pr}_t = \nu_t / \alpha_t$, where ν_t is the turbulent kinematic viscosity and α_t is the turbulent thermal diffusivity.

Finally, the molecular diffusion and the turbulent transport, $\overline{t_{ji} u_i''} - \overline{\rho \frac{1}{2} u_i'' u_i'' u_j''}$, are coupled together and modelled as shown in equation (3.50). Henceforth, σ_ϕ represents the Pr_t for any variable ϕ.

$$\overline{t_{ji} u_i''} - \overline{\tfrac{1}{2} \rho u_i'' u_i'' u_j''} = \left(\mu + \frac{\mu_t}{\sigma_k} \right) \frac{\partial k}{\partial x_j} \tag{3.50}$$

The approximations described above are then introduced in equation (3.40), leading to

$$\begin{aligned} \int_\Theta \left[\frac{\partial}{\partial t} (\overline{\rho} \tilde{E}) + \frac{\partial}{\partial x_j} (\overline{\rho} \tilde{u}_j \tilde{H}) \right] \mathrm{d}\Theta = \int_\Theta \Bigg[\frac{\partial}{\partial x_j} \Bigg[\left(\frac{\mu}{\mathrm{Pr}} + \frac{\mu_t}{\mathrm{Pr}_t} \right) \frac{\partial \tilde{h}}{\partial x_j} + \left(\mu + \frac{\mu_t}{\sigma_k} \right) \frac{\partial k}{\partial x_j} + \\ + \tilde{u}_i \left(\tilde{t}_{ij} + \tau_{ij} \right) \Bigg] \Bigg] \mathrm{d}\Theta \end{aligned} \tag{3.51}$$

At this point, the system of governing equations is still open at μ_t, k and Pr_t. Material properties must also be defined.

3.3 Turbulence modelling

As mentioned earlier, τ_{ij} can be directly solved. But for now, the focus is on using the Boussinesq approximation and modelling the turbulent viscosity. Turbulence models approach this in different ways but generally using the same properties such as the turbulent kinetic energy, the turbulent dissipation rate, ε, and the specific dissipation rate, ω. Each of these variables needs a transport equation and in turbulence terminology, an n-equation model refers to the n additional equations besides the ones expressing the conservation of mass, momentum and energy, needed to close the system.

The mixing length hypothesis proposed by L. Prandtl provides an expression to define the turbulent viscosity based on the assumption that the x-momentum of a fluid remains constant for a length of l_{mix} in the y direction. l_{mix} is the mixing length that is characteristic of each flow geometry along with a characteristic velocity, that must be defined in advance. Ergo, zero equation models where the length and velocity scales are not defined through properties such as k, ε or ω, are not independent of the case of study.

One and two equation models overcome this obstacle by introducing transport equations for history dependent variables that can represent a velocity and a length scale. Specifically,

the two equation models studied in this work define the velocity scale through the turbulent kinetic energy to incorporate non-local and flow history effects in the turbulent viscosity. Its transport equation comes from the transport equation of the trace of the Reynolds stress tensor, shown in equation (3.48), leading to

$$\frac{\partial}{\partial t}(\overline{\rho}k) + \frac{\partial}{\partial x_j}(\overline{\rho}\tilde{u}_j k) = \tau_{ij}\frac{\partial \tilde{u}_i}{\partial x_j} - \overline{t_{ji}\frac{\partial u_i''}{\partial x_j}} + \frac{\partial}{\partial x_j}\left[\overline{t_{ji}u_i''} - \overline{\tfrac{1}{2}\rho u_i'' u_i'' u_j''} - \overline{p'u_j''}\right] - \\ -\overline{u_i''}\frac{\partial \overline{p}}{\partial x_i} + \overline{p'\frac{\partial u_i''}{\partial x_i}} \quad (3.52)$$

with the averaged dissipation rate defined by

$$\overline{\rho}\varepsilon = \overline{t_{ji}\frac{\partial u_i''}{\partial x_j}} \quad (3.53)$$

The molecular diffusion and the turbulent transport are once again simplified through the approximation from equation (3.50) while $\overline{p'u_j''}$ and $\overline{p'(\partial u_i''/\partial x_i)}$ are disregarded due to the lack of knowledge on its behaviour and the believe that it has a minor effect in the flow. The pressure work term $\overline{u_i''}(\partial\overline{p}/\partial x_i)$ is also left out. As a result, equation (3.52) becomes

$$\frac{\partial}{\partial t}(\overline{\rho}k) + \frac{\partial}{\partial x_j}(\overline{\rho}\tilde{u}_j k) = \tau_{ij}\frac{\partial \tilde{u}_i}{\partial x_j} - \overline{\rho}\varepsilon + \frac{\partial}{\partial x_j}\left[\left(\mu + \frac{\mu_t}{\sigma_k}\right)\frac{\partial k}{\partial x_j}\right] \quad (3.54)$$

3.3.1 Spalart-Allmaras

Unlike other turbulence models, the one equation Spalart-Allmaras model [20, 53] directly derives a transport equation for the turbulent viscosity. In this case, the turbulent kinetic energy present in equation (3.47) is disregarded when calculating τ_{ij}:

$$\tau_{ij} \approx 2\mu_t\left(\tilde{S}_{ij} - \frac{1}{3}\tilde{S}_{kk}\delta_{ij}\right) \quad (3.55)$$

The turbulent viscosity is given by

$$\mu_t = \overline{\rho}\tilde{\nu}f_{v1} \quad (3.56)$$

where $\tilde{\nu}$ is the modified turbulent viscosity and the viscous damping function, f_{v1}, is given by

$$f_{v1} = \frac{\chi^3}{\chi^3 + c_{v1}^3}, \quad \chi = \frac{\tilde{\nu}}{\nu} \quad (3.57)$$

where c_{v1} is a constant of the model. The transport equation for $\tilde{\nu}$ includes a production, a destruction and a diffusion term:

$$\frac{\partial}{\partial t}(\overline{\rho}\tilde{\nu}) + \frac{\partial}{\partial x_j}(\overline{\rho}\tilde{u}_j\tilde{\nu}) = P - D + \frac{1}{\sigma_{\tilde{\nu}}}\left[\frac{\partial}{\partial x_j}\left((\mu + \overline{\rho}\tilde{\nu})\frac{\partial \tilde{\nu}}{\partial x_j}\right) + c_{b2}\frac{\partial \tilde{\nu}}{\partial x_i}\frac{\partial \tilde{\nu}}{\partial x_i}\right] \quad (3.58)$$

The production of turbulent viscosity, P, is given by

$$P = c_{b1}\overline{\rho}\hat{S}\tilde{\nu} \quad (3.59)$$

with

$$\hat{S} = \tilde{\Omega} + \frac{\tilde{\nu}}{\kappa^2 d^2} f_{v2}, \quad f_{v2} = 1 - \frac{\chi}{1 + \chi f_{v1}} \quad (3.60)$$

Here, c_{b1} and κ are constants, d is the distance to the wall and $\tilde{\Omega}$ is the mean magnitude of vorticity defined in equation (3.61) where $\tilde{\Omega}_{ij}$ is the mean vorticity.

$$\tilde{\Omega} = \sqrt{2\tilde{\Omega}_{ij}\tilde{\Omega}_{ij}}, \quad \tilde{\Omega}_{ij} = \frac{1}{2}\left(\frac{\partial \tilde{u}_i}{\partial x_j} - \frac{\partial \tilde{u}_j}{\partial x_i}\right) \quad (3.61)$$

The destruction term D is defined as

$$D = c_{w1}\overline{\rho} f_w \left(\frac{\tilde{\nu}}{d}\right)^2 \quad (3.62)$$

where

$$f_w = g\left[\frac{1 + c_{w3}^6}{g^6 + c_{w3}^6}\right]^{1/6}, \quad g = r + c_{w2}(r^6 - r), \quad r = \frac{\tilde{\nu}}{\hat{S}\kappa^2 d^2} \quad (3.63)$$

$$c_{w1} = \frac{c_{b1}}{\kappa^2} + \frac{1 + c_{b2}}{\sigma_{\tilde{\nu}}} \quad (3.64)$$

The constant c_{w1} is here introduced as function of c_{b1} and c_{b2} to balance the production, destruction and diffusion of $\tilde{\nu}$ and the constants c_{w2} and c_{w3} are model specific, listed in Table 3.1 along with the additional constants. This model includes additional terms related

Table 3.1: Spalart-Allmaras model constants [20]

Constant	Value
$\sigma_{\tilde{\nu}}$	2/3
κ	0.4187
c_{b1}	0.1355
c_{b2}	0.622
c_{w2}	0.3
c_{w3}	2
c_{v1}	7.1

to the transition from laminar to turbulent flow. But since the case of study is fully turbulent, such terms can be neglected and are not mentioned here. The following turbulence models are presented in the same manner where only the used terms are presented and discussed.

Ultimately, the three independent unknowns present in the Reynolds tensor have here been replaced by one unknown, μ_t, and equation (3.58). Hence, the system is closed.

3.3.2 Standard $k - \varepsilon$

If k is used to define a velocity scale, a formulation is still needed for the length scale, otherwise user input is still required and the system is not closed:

$$\mu_t = \overline{\rho} k^{1/2} l \quad (3.65)$$

To define the turbulent length scale l, an additional transport equation for the turbulent dissipation rate is introduced, leading to

$$\mu_t \sim \overline{\rho} k^2/\varepsilon, \qquad l \sim k^{3/2}/\varepsilon \quad (3.66)$$

A definition for k is already available in equation (3.54) and one more needs to be formulated for ε. Deriving an exact equation for the turbulent dissipation rate produces more correlation terms than it does for the transport equation of k as [57] demonstrates. As an alternative, it is defined in analogy with equation (3.54), i.e., the dissipation rate equation has generation and destruction terms that are assumed to be proportional to the production and dissipation of k. Still, this approximation represents one of the main weaknesses of ε based models.

As a result, the standard $k - \varepsilon$ model [20, 51] can be written as:

$$\frac{\partial}{\partial t}(\overline{\rho} k) + \frac{\partial}{\partial x_i}(\overline{\rho} \tilde{u}_i k) = \tau_{ij} \frac{\partial \tilde{u}_j}{\partial x_i} - \overline{\rho}\varepsilon + \frac{\partial}{\partial x_j}\left[\left(\mu + \frac{\mu_t}{\sigma_k}\right)\frac{\partial k}{\partial x_j}\right] \quad (3.67)$$

$$\frac{\partial}{\partial t}(\overline{\rho} \varepsilon) + \frac{\partial}{\partial x_i}(\overline{\rho} \tilde{u}_i \varepsilon) = C_{\varepsilon 1} \frac{\varepsilon}{k} \tau_{ij} \frac{\partial \tilde{u}_j}{\partial x_i} - C_{\varepsilon 2} \overline{\rho} \frac{\varepsilon^2}{k} + \frac{\partial}{\partial x_j}\left[\left(\mu + \frac{\mu_t}{\sigma_\varepsilon}\right)\frac{\partial \varepsilon}{\partial x_j}\right] \quad (3.68)$$

The turbulent viscosity is defined by

$$\mu_t = C_\mu \frac{\overline{\rho} k^2}{\varepsilon}, \qquad l = C_\mu k^{3/2}/\varepsilon \quad (3.69)$$

where C_μ is a model constant. The remaining constants of the model are listed in Table 3.2.

Table 3.2: Standard $k - \varepsilon$ model constants [20]

Constant	Value
$C_{\varepsilon 1}$	1.44
$C_{\varepsilon 2}$	1.92
C_μ	0.09
σ_k	1.0
σ_ε	1.3

The model was developed under the assumption that the effects of viscosity on the turbulence structure are negligible which means that it is only valid for fully turbulent flows.

Besides the current version, two additional ε based models are introduced over the next sections.

3.3.3 RNG $k-\varepsilon$

[20, 58] implemented renormalisation group (RNG) methods to account for the different scales of motion and for a more accurate representation of the Pr_t number used both in the turbulent properties and in the energy equation. This modified version of the $k-\varepsilon$ model no longer restricts the Reynolds number and is therefore more accurate and reliable for a wider range of flows than the standard model.

In the RNG $k-\varepsilon$ model, equation (3.69) remains unchanged but the transport equations are slightly altered:

$$\frac{\partial}{\partial t}(\overline{\rho}k)+\frac{\partial}{\partial x_i}(\overline{\rho}\tilde{u}_i k)=\tau_{ij}\frac{\partial \tilde{u}_j}{\partial x_i}-\overline{\rho}\varepsilon+\frac{\partial}{\partial x_j}\left[\left(\psi_k \mu_{eff}\right)\frac{\partial k}{\partial x_j}\right] \quad (3.70)$$

$$\frac{\partial}{\partial t}(\overline{\rho}\varepsilon)+\frac{\partial}{\partial x_i}(\overline{\rho}\tilde{u}_i \varepsilon)=C_{\varepsilon 1}\frac{\varepsilon}{k}\tau_{ij}\frac{\partial \tilde{u}_j}{\partial x_i}-\tilde{C}_{\varepsilon 2}\overline{\rho}\frac{\varepsilon^2}{k}+\frac{\partial}{\partial x_j}\left[\left(\psi_\varepsilon \mu_{eff}\right)\frac{\partial \varepsilon}{\partial x_j}\right] \quad (3.71)$$

Here, $C_{\varepsilon 2}$ is no longer a constant but instead defined by

$$\tilde{C}_{\varepsilon 2}=C_{\varepsilon 2}+\frac{C_\mu \lambda^3(1-\lambda/\lambda_o)}{1+\beta\lambda^3}, \quad \lambda\equiv\frac{k}{\varepsilon}\tilde{S}, \quad \tilde{S}=\sqrt{2\tilde{S}_{ij}\tilde{S}_{ij}} \quad (3.72)$$

where $\tilde{S}$ is the magnitude of the mean strain-rate tensor. For moderately or weakly strained flows, the RNG model produces comparable results to the standard model. However, in regions of large strain, $\lambda>\lambda_0$, there is a negative contribution and the value of $\tilde{C}_{\varepsilon 2}$ decreases. As a result, the overall value of ε increases, reducing k and the turbulent viscosity.

The inverse effective Pr numbers ψ_k and ψ_ε are defined according to the RNG theory [20]:

$$\left|\frac{\psi-1.3929}{\psi_0-1.3929}\right|^{0.6321}\left|\frac{\psi-2.3929}{\psi_0-2.3929}\right|^{0.3679}=\frac{\mu}{\mu_{eff}} \quad (3.73)$$

where $\mu_{eff}=\mu+\mu_t$ and $\psi_0=1.0$. As the Re number increases, ψ_k and ψ_ε will tend to 1.393. The constants employed in this model are listed in Table 3.3.

Table 3.3: RNG $k-\varepsilon$ model constants [20]

Constant	Value
$C_{\varepsilon 1}$	1.42
$C_{\varepsilon 2}$	1.68
C_μ	0.0845
β	0.012
λ_0	4.38

3.3.4 Realisable $k-\varepsilon$

A common issue with the previous $k-\varepsilon$ models is that they do not always fulfil the constraint of positivity of the normal Reynolds stress terms. Let us once again consider equation (3.47)

to define the normal Reynolds stresses:

$$\overline{u_i''^2} = -2\nu_t\left(\tilde{S}_{ii} - \frac{1}{3}\tilde{S}_{kk}\right) + \frac{2}{3}k \quad (3.74)$$

If equation (3.69) is now used to replace ν_t, it is visible that $\overline{u_i''^2}$, which must be positive, becomes negative when the strain is large enough to satisfy

$$\frac{k}{\varepsilon}\left(\tilde{S}_{ii} - \tilde{S}_{kk}\right) > \frac{1}{3C_\mu} \approx 3.7 \quad (3.75)$$

for the standard $k-\varepsilon$, as an example.

The realisable $k-\varepsilon$ model [20,57] overcomes this problem by formulating a flow dependent C_μ and by applying a new definition for ε obtained from the exact equation for the transport of the mean square vorticity fluctuation $\overline{\omega_i'\omega_i'}$. For high Reynolds numbers the assumption $\varepsilon = \nu\overline{\omega_i'\omega_i'}$ is valid, as shown by [57], and can be used to derive a dissipation rate transport equation leading to

$$\frac{\partial}{\partial t}(\overline{\rho}k) + \frac{\partial}{\partial x_j}(\overline{\rho}\tilde{u}_j k) = \tau_{ij}\frac{\partial \tilde{u}_i}{\partial x_j} - \overline{\rho}\varepsilon + \frac{\partial}{\partial x_j}\left[\left(\mu + \frac{\mu_t}{\sigma_k}\right)\frac{\partial k}{\partial x_j}\right] \quad (3.76)$$

$$\frac{\partial}{\partial t}(\overline{\rho}\varepsilon) + \frac{\partial}{\partial x_j}(\overline{\rho}\tilde{u}_j \varepsilon) = C_1\overline{\rho}S\varepsilon - C_2\frac{\overline{\rho}\varepsilon^2}{k+\sqrt{\nu\varepsilon}} + \left[\left(\mu + \frac{\mu_t}{\sigma_\varepsilon}\right)\frac{\partial \varepsilon}{\partial x_j}\right] \quad (3.77)$$

In contrast with the previous versions, the production of ε is no longer based on the production of k. Equation (3.69) is once again used to define μ_t in which

$$C_\mu = \frac{1}{A_0 + A_s U^* k/\varepsilon} \quad (3.78)$$

A_0 is listed in Table 3.4 along with the remaining constants while A_s, U^* and C_1 are given by

$$U^* = \sqrt{\tilde{S}_{ij}\tilde{S}_{ij} + \tilde{\Omega}_{ij}\tilde{\Omega}_{ij}} \quad (3.79)$$

$$A_s = \sqrt{6}\cos\xi \quad (3.80)$$

$$\xi = \frac{1}{3}\arccos(\sqrt{6}\chi), \quad \chi = \frac{\tilde{S}_{ij}\tilde{S}_{jk}\tilde{S}_{ki}}{\hat{S}^3}, \quad \hat{S} = \sqrt{\tilde{S}_{ij}\tilde{S}_{ij}} \quad (3.81)$$

$$C_1 = \max\left[0.43, \frac{\eta}{5+\eta}\right], \quad \eta = \frac{\tilde{S}k}{\varepsilon} \quad (3.82)$$

Table 3.4: Realisable $k-\varepsilon$ model constants [20]

Constant	Value
σ_k	1
σ_ε	1.2
C_2	1.9
A_0	4.04

3.3.5 Standard $k-\omega$

In the $k-\omega$ model, the length scale is the specific dissipation rate, ω, such that

$$\mu_t \sim \overline{\rho} k/\omega, \qquad l \sim k^{1/2}/\omega, \qquad \varepsilon \sim k\omega \quad (3.83)$$

The presented version of the $k-\omega$ model from [20] is an improvement over the original 1998 version proposed by Wilcox [59]. A more recent version of the model is already available in [56] to deal with the ill behaviour of the ω in free stream regions by means of a cross-diffusion term. However, the used modified version claims to achieve a similar goal.

The turbulent dissipation rate is replaced by the dissipation per unit time or specific dissipation rate defined as $\omega = \varepsilon/k$. The transport equations for the turbulent variables in this model are written as

$$\frac{\partial}{\partial t}(\overline{\rho}k) + \frac{\partial}{\partial x_j}(\overline{\rho}\tilde{u}_j k) = \tau_{ij}\frac{\partial \tilde{u}_i}{\partial x_j} - \overline{\rho}\beta^* f_{\beta^*} k\omega + \frac{\partial}{\partial x_j}\left[\left(\mu + \sigma_k \frac{\overline{\rho}k}{\omega}\right)\frac{\partial k}{\partial x_j}\right] \quad (3.84)$$

$$\frac{\partial}{\partial t}(\overline{\rho}\omega) + \frac{\partial}{\partial x_j}(\overline{\rho}\tilde{u}_j \omega) = \frac{\omega}{k}\tau_{ij}\frac{\partial \tilde{u}_i}{\partial x_j} - \overline{\rho}\beta f_\beta \omega^2 + \frac{\partial}{\partial x_j}\left[\left(\mu + \sigma_\omega \frac{\overline{\rho}k}{\omega}\right)\frac{\partial \omega}{\partial x_j}\right] \quad (3.85)$$

In equation (3.84), β^* and σ_k are constant and unlike in the 2006 Wilcox version where the cross diffusion term $(\partial k/\partial x_j)(\partial\omega/\partial x_j)$ appears in the transport equation of ω, it is here introduced in the dissipation of the turbulent kinetic energy through f_{β^*}:

$$f_{\beta^*} = \begin{cases} 1 & , \chi_k \leq 0 \\ \frac{1+680\chi_k^2}{1+400\chi_k^2} & , \chi_k > 0 \end{cases}, \qquad \chi_k = \frac{1}{\omega^3}\frac{\partial k}{\partial x_j}\frac{\partial \omega}{\partial x_j} \quad (3.86)$$

Equation (3.85) contains an additional element f_β that is defined in equation (3.87) and the new model constants are available in Table 3.5.

$$f_\beta = \frac{1+70\chi_\omega}{1+80\chi_\omega}, \qquad \chi_\omega = \left|\frac{\tilde{\Omega}_{ij}\tilde{\Omega}_{jk}\tilde{S}_{ki}}{(\beta^*\omega)^3}\right| \quad (3.87)$$

Additional terms related to low Reynolds numbers corrections and compressible effects are available for this model but are neglected for the current study. Also, and much like in the realisable $k-\varepsilon$ model, an attempt is made to reducing the round-jet anomaly by sensitising

Table 3.5: Standard $k-\omega$ model constants [20]

Constant	Value
σ_k	2.0
σ_ω	2.0
β^*	0.09
β	0.072

the dissipation of ω to the mean deformation of the flow through f_β and χ_ω. The predictions for k and ω outside of the shear layer remain on the biggest setbacks of this model, despite the introduction of a cross diffusion term.

3.3.6 SST $k-\omega$

After the proposal of the Wilcox $k-\omega$ model, [60] developed the shear-stress transport (SST) $k-\omega$ model to retain the robust and accurate formulation of the Wilcox model inside the shear layer while taking advantage of the freestream qualities of the $k-\varepsilon$ model in the farfield. To achieve this, the transport equation for ε is converted into a similar formulation as that of ω, both are multiplied by a blending function and finally added together. This blending function, F_1, is designed to be one in the viscous sublayer of the boundary layer and tend to zero in the log-law region ($y^+ > 70$), thus switching from the $k-\omega$ to the $k-\varepsilon$ based coefficients in the proper moment. With this, the transport equations are written as

$$\frac{\partial}{\partial t}(\overline{\rho}k) + \frac{\partial}{\partial x_j}(\overline{\rho}\tilde{u}_j k) = \tau_{ij}\frac{\partial \tilde{u}_i}{\partial x_j} - \beta^*\overline{\rho}k\omega + \frac{\partial}{\partial x_j}\left[(\mu + \sigma_k\mu_t)\frac{\partial k}{\partial x_j}\right] \quad (3.88)$$

$$\begin{aligned}\frac{\partial}{\partial t}(\overline{\rho}\omega) + \frac{\partial}{\partial x_j}(\overline{\rho}\tilde{u}_j\omega) = \frac{\gamma}{\nu_t}\tau_{ij}\frac{\partial \tilde{u}_i}{\partial x_j} - \beta\overline{\rho}\omega^2 + \left[(\mu + \sigma_\omega\mu_t)\frac{\partial \omega}{\partial x_j}\right] + \\ +(1-F_1)2\overline{\rho}\frac{1}{\omega\sigma_{\omega 2}}\frac{\partial k}{\partial x_j}\frac{\partial \omega}{\partial x_j}\end{aligned} \quad (3.89)$$

The constants σ_k, σ_ω, γ and β, represented by ϕ, are affected by the blending function F_1 and ruled by

$$\phi = F_1\phi_1 + (1-F_1)\phi_2 \quad (3.90)$$

where ϕ_1 and ϕ_2 represent the analogous $k-\omega$ and $k-\varepsilon$ constants, respectively. These constants, with the corresponding subscripts, are listen in Table 3.6. Additionally, γ is defined by

$$\gamma_1 = \beta_1/\beta^* - \kappa^2/\sigma_{\omega 1}\sqrt{\beta^*}, \quad \gamma_2 = \beta_2/\beta^* - \kappa^2/\sigma_{\omega 2}\sqrt{\beta^*} \quad (3.91)$$

and the blending function is defined by

$$F_1 = \tanh(\arg_1^4), \qquad \arg_1 = \min\left[\max\left(\frac{\sqrt{k}}{0.09\omega d}, \frac{500\nu}{d^2\omega}\right), \frac{4\rho k}{\sigma_{\omega 2}CD_\omega^+ d^2}\right] \quad (3.92)$$

where d is the distance to the closest surface and CD_ω^+ is the positive part of the cross-diffusion term:

$$CD_\omega^+ = \max\left(2\rho\frac{1}{\omega\sigma_{\omega 2}}\frac{\partial k}{\partial x_j}\frac{\partial \omega}{\partial x_j}, 10^{-10}\right) \quad (3.93)$$

The final alteration is in the turbulent viscosity formulation that becomes

$$\mu_t = \frac{\overline{\rho}k}{\omega}\frac{1}{\max[1, (\tilde{S}F_2)/(a_1\omega)]} \quad (3.94)$$

$$F_2 = \tanh(\arg_2^2), \quad \arg_2 = \max\left(2\frac{\sqrt{k}}{0.09\omega d}, \frac{500\mu}{d^2\omega\overline{\rho}}\right) \quad (3.95)$$

Contrary to what the previous models do, this provides two different definitions for μ_t in an attempt to better approximate the Reynolds stresses through a blending function, F_2, that is equal to zero in free shear layers and one in boundary layers. In the latter region, τ is assumed to be proportional to k:

$$\tau = \overline{\rho}a_1 k \quad (3.96)$$

Combining this with the definition of τ taken from the Boussinesq approximation, in equation (3.97), equation (3.94) is obtained.

$$\tau \approx \mu_t \tilde{S} \quad (3.97)$$

By guaranteeing that the condition from (3.96) is satisfied inside the boundary layer, this model aims to achieve better results in near wall regions. However, when in free shear regions, there is actually no improvement since the definition of μ_t returns to $\overline{\rho}k/\omega$.

Table 3.6: SST $k-\omega$ model constants [20]

Constant	Value
σ_{k1}	1.176
σ_{k2}	1.0
$\sigma_{\omega 1}$	2.0
$\sigma_{\omega 2}$	1.168
β_1	0.075
β_2	0.0828
β^*	0.09
κ	0.4187
a_1	0.31

3.3.7 Reynolds Stress-BSL

Second-order turbulence models abandon the Boussinesq approximation in favour of a transport equation for τ_{ij} that is coupled with an equation for either ε or ω. Since the latter is still a modelled equation, it is one of the largest sources for loss of accuracy in this model. The

other point of concern are the assumptions made to close the τ_{ij} transport equation. Deriving the equation for the Reynolds stresses yields

$$\begin{aligned}\frac{\partial \tau_{ij}}{\partial t} + \frac{\partial}{\partial x_k}(\tilde{u}_k \tau_{ij}) = -\tau_{ik}\frac{\partial \tilde{u}_j}{\partial x_k} - \tau_{jk}\frac{\partial \tilde{u}_i}{\partial x_k} - \overline{\rho}\varepsilon_{ij} + \overline{\rho}\Pi_{ij} + \\ + \frac{\partial}{\partial x_k}\left[\mu\frac{\partial \overline{u_i'' u_j''}}{\partial x_k} - \overline{\rho} C_{ijk}\right]\end{aligned} \tag{3.98}$$

where the pressure strain, the dissipation and the turbulent diffusion are defined in equations (3.101), (3.99) and (3.100) respectively, and need to be approximated.

$$\overline{\rho}\varepsilon_{ij} = \overline{t_{kj}\frac{\partial u_i''}{\partial x_k} + t_{ki}\frac{\partial u_j''}{\partial x_k}} \tag{3.99}$$

$$\overline{\rho} C_{ijk} = \overline{\rho u_i'' u_j'' u_k''} + \overline{p' u_i''}\delta_{jk} + \overline{p' u_j''}\delta_{ik} \tag{3.100}$$

$$\overline{\rho}\Pi_{ij} = \overline{p'\left(\frac{\partial u_i''}{\partial x_j} + \frac{\partial u_j''}{\partial x_i}\right)} \tag{3.101}$$

According to [20], ε_{ij} is approximated by

$$\varepsilon_{ij} = \frac{2}{3}\beta^* k\omega\delta_{ij} \tag{3.102}$$

Unlike in expression (3.99), here only the trace of ε_{ij} is considered, i.e., this approximation implies that the motion in the small scales is essentially isotropic and therefore only valid for high Re numbers. For lower Re, additional considerations are needed as discussed by [61]. Also, in equation (3.102) β^* is a constant while k and ω are solved using the BSL $k-\omega$ model from [60] similar to the version presented in section 3.3.6. The only difference being that μ_t is defined as in equation (3.83) and the model constants are replaced by those from Table 3.7. Additionally, the turbulent diffusion C_{ijk} is defined according to [62]:

$$C_{ijk} = \frac{\mu_t}{\overline{\rho}\sigma_k}\frac{\partial \overline{u_i'' u_j''}}{\partial x_k} \tag{3.103}$$

where $\sigma_k = 0.82$.

To achieve an approximation for the pressure strain term, the pressure fluctuation p' is divided into p'_{slow} and p'_{rapid} from which a slow and a fast pressure strain term spawn. By applying the LRR model from [63], the sum of both terms gives

$$\begin{aligned}\Pi_{ij} = -\beta^* C_1 \omega\left(\overline{u_i'' u_j''} - \frac{2}{3}k\delta_{ij}\right) - \hat{\alpha}\left(P_{ij} - \frac{1}{3}P_{kk}\delta_{ij}\right) - \hat{\beta}\left(D_{ij} - \frac{1}{3}P_{kk}\delta_{ij}\right) - \\ - \hat{\gamma} k\left(S_{ij} - \frac{1}{3}S_{kk}\delta_{ij}\right)\end{aligned} \tag{3.104}$$

with

$$P_{ij} = -\overline{u_i'' u_m''}\frac{\partial \tilde{u}_j}{\partial x_m} - \overline{u_j'' u_m''}\frac{\partial \tilde{u}_i}{\partial x_m}, \quad D_{ij} = -\overline{u_i'' u_m''}\frac{\partial \tilde{u}_m}{\partial x_j} - \overline{u_j'' u_m''}\frac{\partial \tilde{u}_m}{\partial x_i} \quad (3.105)$$

$$\hat{\alpha} = (8 + C_2)/11, \quad \hat{\beta} = (8C_2 - 2)/11, \quad \hat{\gamma} = (60C_2 - 4)/55 \quad (3.106)$$

In the end, the approximations from equations (3.102), (3.103) and (3.104) are introduced into equation (3.98) and the model constants are obtained from Table 3.7.

Table 3.7: Reynolds Stress-BSL model constants [20]

Constant	Value
σ_{k1}	2.0
$\sigma_{\omega 1}$	2.0
β_1	0.075
σ_{k2}	1.0
$\sigma_{\omega 2}$	1.168
β_2	0.0828
β^*	0.09
κ	0.4187
C_1	1.8
C_2	0.52

3.3.8 Additional considerations on heat transfer modelling

Heat transfer is modelled according to equation (3.51) with small alterations in regards to the Pr_t, depending on the turbulence model. It seems that this variable has a considerable impact on the development of the flow structure. [64] concluded that a constant value of 1 for the Pr_t number provides the best approximation when compared to variable Pr_t formulations, and [34] arrives at the same conclusion when comparing his numerical results to the experimental data. For this reason, the Pr_t is set to 1 in the energy equation (3.51). Nevertheless, [64] demonstrated that a variable Pr_t number is particularly important in the transition region and the RNG $k - \varepsilon$ is the only model used where this ratio is not a constant neither in the energy equation nor in the transport equations of the turbulent properties. In this case, the term

$$\left(\frac{\mu}{\mathrm{Pr}} + \frac{\mu_t}{\mathrm{Pr}_t}\right)\frac{\partial \tilde{h}}{\partial x_j} \quad (3.107)$$

is replaced with

$$\kappa_{eff}\frac{\partial \tilde{T}}{\partial x_j} \quad (3.108)$$

where the effective thermal conductivity κ_{eff} is defined as

$$\kappa_{eff} = \psi c_p \mu_{eff} \quad (3.109)$$

Here, the inverse effective Pr number, ψ, is calculated using equation (3.73) with $\psi_0 = 1/\text{Pr}$. This approach gives the RNG $k-\varepsilon$ model an advantage over other alternatives where the turbulent Pr number is set as a constant.

3.4 Equation of State

In the supercritical regime, physical properties can vary drastically and cannot be defined by simple relations. One such property is the density and, as the test case is incompressible, the main concern is to establish a reliable relation between density and temperature variations. For this, three EoS are implemented. As seen in Figure 3.1, in the vicinity of the critical point the PR and the SRK EoS show a different behaviour. This error affects the prediction of the jet structure and its impact should therefore be assessed. With this in mind, version 9.1 of the National Institute of Standards and Technology (NIST) Reference Fluid Thermodynamic and Transport Properties Database (REFPROP) [65] is directly linked to FLUENT®. The nitrogen properties stored in this library are calculated using the multi-parameter EoS from [19] and the high accuracy of this method means that it can be used as a benchmark for comparison and evaluation of the behaviour of the two cubic EoS.

3.4.1 Soave-Redlich-Kwong EoS

Unlike in the ideal gas equation, two parameter Equations of State consider both the finite volume of the molecules and the attraction forces between one another through the parameters b and a, respectively. [21] introduced a modified version to the original Redlich-Kwong equation [66]:

$$p = \frac{RT}{v-b} - \frac{a(T)}{v(v+b)} \quad (3.110)$$

with v as the molar volume and R as the molar gas constant. The modifications from Soave lay mainly with the dependence of a on T_c, to improve the behaviour in the supercritical region, and on the acentric factor, ω, to deal with the polarity of individual species. The variables a and b are defined by

$$a = a(T_c)\zeta(\tau,\omega), \quad a(T_c) = 0.42747\frac{R^2T_c^2}{p_c}, \quad b = 0.08664\frac{RT_c}{p_c} \quad (3.111)$$

where τ is the inverse reduced temperature, T_c/T, and the dimensionless parameter $\zeta(\tau,\omega)$ is defined as

$$\zeta(\tau,\omega)^{0.5} = 1 + m(1-\tau^{-0.5}), \quad m = 0.480 + 1.574\omega - 0.176\omega^2 \quad (3.112)$$

At the critical point, $\zeta(\tau,\omega)$ becomes unity and the definition for a becomes similar to that of the Redlich-Kwong EoS. To apply this EoS, one only needs the critical constants and the acentric factor which goes to show the simplicity of this relation, especially when compared to multi-parametric models. For the case of nitrogen, the critical properties are listed in

Table 2.1 and the acentric factor is equal to 0.0372.

3.4.2 Peng-Robinson EoS

In the quest for a more reliable Equation of State, [22] proposed a new EoS with an improved prediction of the liquid density values:

$$p = \frac{RT}{v-b} - \frac{a(T)}{v(v+b)+b(v-b)} \tag{3.113}$$

where a and b are defined by

$$a = a(T_c)\zeta(\tau,\omega), \quad a(T_c) = 0.45724\frac{R^2T_c^2}{p_c}, \quad b = 0.07780\frac{RT_c}{p_c} \tag{3.114}$$

and the factor $\zeta(\tau,\omega)$ is

$$\zeta(\tau,\omega)^{0.5} = 1 + m(1-\tau^{-0.5}), \quad m = 0.37464 + 1.54226\omega - 0.26992\omega^2 \tag{3.115}$$

The coefficients of both EoS have a similar structure. But, as the comparison analysis from [67] suggests, the PR EoS has a higher accuracy from the critical point up to $2\rho_c$ after which the predictions of the SRK equation are preferable. For the region between $0.4\rho_c < \rho < \rho_c$ it is not exactly clear which is better suited but this will come again into question in section 5.1.1. In any case, both tend to similar values at lower densities as shown in Figure 3.1. Still, the author argues that no analytical equation can properly define the critical region since it does not have an analytical nature. The path to increased accuracy is through an EoS possessed of parameters determined from data fitting methods.

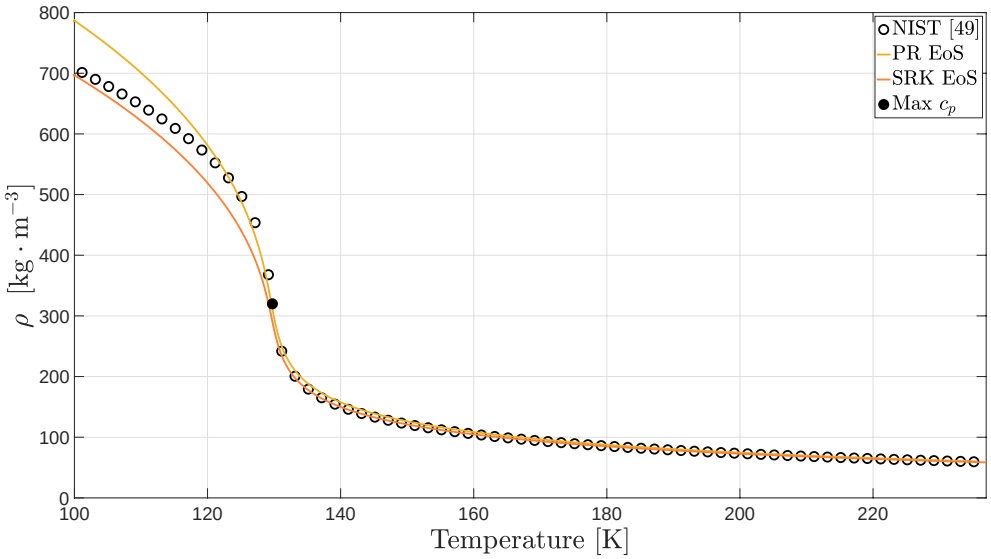

Figure 3.1: Comparison of density values obtained from the PR EoS, the SRK EoS and the NIST database at 4 MPa [49]

3.4.3 A reference EoS for nitrogen

The EoS presented by [19] is based on the Helmholtz energy, F, which is then normalised and set as a function of τ and $\delta = \rho/\rho_c$:

$$\frac{F(\rho,T)}{RT} = f(\delta,\tau) = f^0(\delta,\tau) + f^r(\delta,\tau) \quad (3.116)$$

The first right hand-side term refers to the ideal gas contribution to the Helmholtz energy while the second represents the residual Helmholtz energy corresponding to the intermolecular forces considered in a real gas formulation. The ideal gas contribution is defined in equation (3.117), the residual addition is shown in equation (3.118) and the corresponding constants are listed in [19]. Thermodynamic properties can then be calculated based on the derivatives of these two terms.

$$f^0(\delta,\tau) = \ln(\delta) + a_1\ln(\tau) + a_2 + a_3\tau + a_4\tau^{-1} + a_5\tau^{-2} + a_6\tau^{-3} + \\ + a_7\ln\left(1-\exp[-a_8\tau]\right) \quad (3.117)$$

$$f^r(\delta,\tau) = \sum_{k=1}^{6} N_k\delta^{i_k}\tau^{j_k} + \sum_{k=7}^{32} N_k\delta^{i_k}\tau^{j_k}\exp[-\delta^{l_k}] + \sum_{k=33}^{36} N_k\delta^{i_k}\tau^{j_k}\exp[-\phi_k(\delta-1)^2 - \\ -\beta_k(\tau-\gamma_k)^2] \quad (3.118)$$

The coefficients specific to this EoS are obtained through data fitting methods based on experimental measurements from a series of authors and for a wide range of temperatures and pressures. Its accuracy is, therefore, considerably higher in the supercritical region than the PR or the SRK EoS as depicted in Fig 3.1 where the information obtained from the NIST database is calculated through this EoS, [49]. Additionally, the author reports an average absolute error (AAD%), defined in equation (3.119), for the density values of no more than 0.042% for $0.6 < \delta < 1.5$ when compared to experimental measurements. This level of accuracy provides a good point of reference to determine the influence of the cubic Equations of State on the development of a supercritical jet.

$$\text{AAD\%} = \frac{\sum_{i=1}^{n}|\phi_i - \phi_i^{exact}|}{n} \times 100 \quad (3.119)$$

3.5 Transport properties

Transport properties have a direct impact on the governing equations through such terms as those in equations (3.19) and (3.41) and must, therefore, be properly defined. Their strong variation is already discussed in section 2.1 when it is made clear that there is a sharp drop both in molecular viscosity and thermal conductivity as temperature approach supercritical values. To overcome this non-linear behaviour, the work from [68] is used to define both μ and κ regardless of the EoS used. This is already implemented into the REFPROP database, but when using the cubic EoS, UDFs are written to defined these variables. In any case, the

associated error with these formulations is of around 2% for both the molecular viscosity and thermal conductivity.

The molecular viscosity is split into an ideal gas and a residual contribution and is defined in equation (3.120) in $\mu\mathrm{Pa}\cdot\mathrm{s}$.

$$\mu = \mu^0(T) + \mu^r(\delta,\tau) \quad (3.120)$$

The ideal and the residual contributions are given by

$$\mu^0(T) = \frac{0.0266958\sqrt{MT}}{\sigma^2\Phi(T^*)}, \qquad \mu^r(\tau,\delta) = \sum_{k=1}^{5} N_k \delta^{i_k}\tau^{j_k}\exp\left[-\gamma_k\delta^{l_k}\right] \quad (3.121)$$

where M is the molar mass and σ is the Lennard-Jones size parameter, listed in Table 3.10, while $\Phi(T^*)$ is

$$\Phi(T^*) = \exp\left[\sum_{k=0}^{4} b_k\big(\ln(T^*)\big)\right], \qquad T^* = \frac{T}{\theta} \quad (3.122)$$

with θ as the Lennard-Jones energy parameter and γ_k being zero if $l_k = 0$ and one if $l_k \neq 0$. Finally, the coefficients for equation (3.121) and equation (3.122) are listed in Table 3.8. Similarly, the thermal conductivity, expressed in equation (3.123) in $\mathrm{mW}\cdot\mathrm{m}^{-1}\cdot\mathrm{K}^{-1}$, is divided into an ideal gas contribution, a residual contribution and an additional critical enhancement term, only applied through the REFPROPv9.1 database.

Table 3.8: Coefficients of the viscosity equation [68]

k	b_k	N_k	i_k	j_k	l_k
0	0.431	-	-	-	-
1	-0.4623	10.72	2	0.1	0
2	0.08406	0.03989	10	0.25	1
3	0.005341	0.001208	12	3.2	1
4	-0.00331	-7.402	2	0.9	2
5	-	4.620	1	0.3	3

$$\kappa = \kappa^0(T) + \kappa^r(\delta,\tau) + \kappa^c(\delta,\tau) \quad (3.123)$$

The ideal gas and the residual contributions are then given by

$$\kappa^0 = N_1\left[\frac{\mu^0(T)}{1\times10^{-6}}\right] + N_2\tau^{j_2} + N_3\tau^{j_3}, \quad \kappa^r = \sum_{i=4}^{n} N_k\delta^{i_k}\tau^{j_k}\exp\left[-\gamma_k\delta^{l_k}\right] \quad (3.124)$$

for which the coefficients N_k, τ^{j_k} and δ^{i_k} are listed in Table 3.9, while γ_k holds the same meaning as it did in equation (3.121). Finally, the critical enhancement term is defined as

$$\kappa^c = \rho c_p \frac{k_B R_0 T}{6\pi\xi\mu}(\hat{\Phi} - \hat{\Phi}_0) \quad (3.125)$$

Here, the molecular viscosity is retrieved from equation (3.120) while $\tilde{\Phi}$, $\tilde{\Phi}_0$ and ξ are

$$\hat{\Phi} = \frac{2}{\pi}\left[\left(\frac{c_p - c_v}{c_p}\right)\tan^{-1}(\xi/q_D) + \frac{c_v}{c_p}(\xi/q_D)\right] \quad (3.126)$$

$$\hat{\Phi}_0 = \frac{2}{\pi}\left(1 - \exp\left[-\frac{1}{(\xi/q_D)^{-1} + \frac{1}{3}(\xi/q_D)^2\delta^{-2}}\right]\right) \quad (3.127)$$

$$\xi = \xi_0\left[\frac{\tilde{\chi}(T,\rho) - \tilde{\chi}(T_0,\rho)(T_0/T)}{\Gamma}\right]^{\mathrm{v}/\gamma}, \qquad \tilde{\chi}(T,\rho) = \frac{p_c\delta}{\rho_c}\left(\frac{\partial\rho}{\partial p}\right)_T \quad (3.128)$$

The isochoric and isobaric specific heats, c_v and c_p, as well as $\tilde{\chi}$ are dependent on the used EoS and the remaining parameters are available in Tables 2.1 and 3.10, though if ξ is negative then κ^c is set to zero.

Table 3.9: Coefficients of the thermal conductivity equation [68]

k	N_k	i_k	j_k	l_k
1	1.511	-	-	-
2	2.117	-	-1.0	-
3	-3.332	-	-0.7	-
4	8.862	1	0.0	0
5	31.11	2	0.03	0
6	-73.13	3	0.2	1
7	20.03	4	0.8	2
8	-0.7096	8	0.6	2
9	0.2672	10	1.9	2

Table 3.10: Parameters of the viscosity and thermal conductivity equations

Properties	Value
T_0 [K]	252.384
M [g · mol^{-1}]	28.01348
σ [nm]	0.3656
θ [K]	98.94
q_D [nm]	0.40
ξ_0 [nm]	0.17
k_B [J · K^{-1}]	1.380658 × 10^{-23}
R [J · mol^{-1} · K^{-1}]	8.3145
R_0	1.01
Γ	0.055
γ	1.2415
v	0.63

3.6 Caloric properties

For the SRK and the PR EoS, the isobaric specific heat is calculated as the sum of the departure specific heat with the ideal contribution, implemented through a UDF in FLUENT®.

This ideal contribution is taken from [19] and is also used to obtain equation (3.117). According to the author, this definition provides an average error of 0.05% for temperatures below $900\,\mathrm{K}$. c_p^0 is described in equation (3.129), where $u = 3364.011/T$ K, and c_p^r is calculated as in equation (3.130).

$$\frac{c_p^0}{R} = 3.5 + 3.066469 \times 10^{-6}T + 4.701240 \times 10^{-9}T^2 - 3.987984 \times 10^{-13}T^3 + \\ +1.012941\frac{u^2\exp(u)}{[\exp(u)-1]^2} \tag{3.129}$$

$$c_p^r = c_v^r - R - T\frac{(\partial V/\partial T)^2}{\partial V/\partial P} \tag{3.130}$$

[20] states that the departure isochoric specific heat, c_v^r, is calculated by differentiating the equation for the departure of the internal energy with respect to the temperature while the other derivates come from differentiating equation (3.110) or (3.113). Ultimately, when using a cubic EoS, the isobaric specific heat is

$$c_p = c_p^0 - \frac{c_p^r}{M} \tag{3.131}$$

When using equation (3.116), the isobaric specific heat is defined through equation (3.132) with each individual term defined in [19].

$$c_p = c_v + R\frac{\left[1+\delta(\partial f^r)/(\partial\delta)_\tau - \delta\tau(\partial^2 f^r)/(\partial\delta\partial\tau)\right]^2}{\left[1+2\delta(\partial f^r)/(\partial\delta)_r + \delta^2(\partial^2 f^r)/(\partial\delta^2)_\tau\right]} \tag{3.132}$$

3.7 Summary

We began this chapter by establishing how the dynamics of a moving fluid can be predicted through the transport equations for the conserved quantities. Sadly, the computational resources currently available do not practically allow for the direct resolution of these equations. The introduction of time-averaging methods solves this problem but leads to another by introducing the Reynolds stresses, the closure of the system of governing equations. At this point, turbulence modelling comes in to predict the fluctuations in the velocity field. Seven different models are introduced that can be split into two main categories, first and second-order models. The first-order models mentioned make use either of one or of two additional turbulent variables while the one second-order model directly resolves the Reynolds stress terms. Moreover, due to the implications of the supercritical regime, we introduce three EoS to predict density values at two distinct accuracy levels. Depending on which is chosen, values are either calculated in real time or retrieved from a real gas library to prevent excessive computational costs. Accurate formulations for the transport properties and for the specific heat capacity are also introduced, where the later is dependent on the EoS used. With an established mathematical model, we now bring the reader into context with

the experimental test conditions and the numerical setup which will lead to a solution in a discretised domain.

Chapter 4

Implementation

The governing equations we discussed in the last chapter can be affected by a respectable amount of error originated from the approximations we made so far. While this is one of the main points of interest in this study, it is not the only source of error. Once the governing equations are defined, they must be applied to a finite computational domain in a process that is affected by numerical error. In this chapter, we describe the discretisation methods selected to reduce this error to a minimum. We then move on to discussing the order in which the equations are calculated and the relaxation settings used to increase stability.

The first section, however, is dedicated to our reference test case which dictates the computational domain geometry and the boundary conditions. The chapter then finishes with a small comparison to determine the number of calculation points needed to achieve mesh independency.

4.1 Test cases

As was already discussed, the test cases from [27] are the basis of comparison for this numerical study. In particular, case 3 and case 4 are investigated where cold nitrogen is injected into a chamber at ambient temperature with 4 windows for optical access. The conditions of cases 3 and 4 are listed in Table 4.1, where the subscripts hold the same meaning as they do in equation (2.2).

Table 4.1: Test conditions [27, 49]

Case	p_∞ [MPa]	u_0 [m/s]	T_0 [K]	T_∞ [K]	ρ_0 [kg/m^3]	ρ_∞ [kg/m^3]
3	3.97	4.9	126.9	297	457.82	45.24
4	3.98	5.4	137	297	164.37	45.36

The test chamber is depicted in Figure 4.1 where the injector measures $90\,\mathrm{mm}$ in length and $2.2\,\mathrm{mm}$ in diameter and the pressurised chamber measures $122\,\mathrm{mm}$ in diameter with a length to injector diameter ratio ($\mathrm{x/d}$) greater than 40. The chamber wall is heated to remain at a constant temperature of $297\,\mathrm{K}$ but neither the injector wall nor the faceplate are heated. The experiment starts with the injector at ambient temperature and during the injection of the liquid nitrogen, it begins to cool down as the fluid heats up. When the fluid reaches the target temperature, the experiment records the Raman or the Shadowgraph images as described by [69]. Since the time needed to obtain the Raman and Shadowgraph images is

small when compared to the time the injector needs to cool down, a quasi steady state flow is considered.

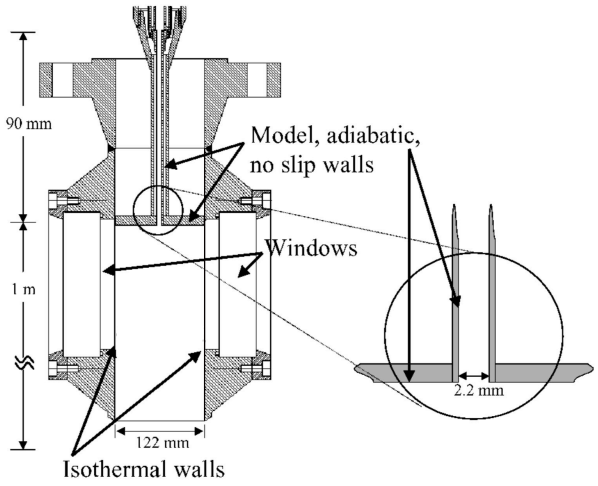

Figure 4.1: Test chamber [27]

The author measures three different temperature sets. The first one, T_1, at the entry of the injector and the other two, T_a and T_b, with a thermocouple at the injector exit. T_a is determined with the thermocouple placed orthogonally to the injector axis where it is only partially covered by the flow. Consequently, the measured temperature is higher than T_b, which is measured with the thermocouple aligned with the jet and placed $1\,\mathrm{mm}$ inside the injector. The author argues that since the temperature at the centre should be lower than the temperature at the wall, this second measure is underestimated. In either case, the two measures are performed in a separate test not to influence the jet flow. For now, T_a is used as the injection temperature.

It is worth noting that velocity values at the injector exit provided by [27] are not measured, but calculated instead. These are based on the chamber pressure, the measured injection mass flow and the temperature at the exit of the injector. It is referred to as the averaged jet velocity at the injector outlet. If one is to simulate the injector while considering an adiabatic injector wall, it is logical to apply u_0 uniformly at the injector inlet and expect a velocity profile at its outlet for which the average velocity is still u_0.

4.2 Numerical setup

This section is dedicated to the numerical methods implemented to properly apply the governing equations to a discretised domain. The test geometry, the mesh and its boundary conditions are initially discussed, followed by a small explanation of the algorithm defining the order of calculation of the equations as well as the pressure-velocity coupling method. Afterwards, the main traits of the employed discretisation schemes are discussed and finally, we present an independence study for the grid resolution and relaxation factors.

4.2.1 Geometry and meshing

A two-dimensional axisymmetric geometry is preferred over a three-dimensional one to reduce computational costs. Based on the experimental setup from [27] depicted in Figure 4.1, the test domain is that in Figure 4.2. The diameter of the chamber and of the injector are of $122\,\mathrm{mm}$ and $2.2\,\mathrm{mm}$ respectively, while measuring in length $250\,\mathrm{mm}$ and $90\,\mathrm{mm}$ each. Assuming that the chamber is vertically aligned in the test experiments from [27], the parameter f_x in equation (3.39) is set to $9.81\,\mathrm{m}\cdot\mathrm{s}^{-2}$.

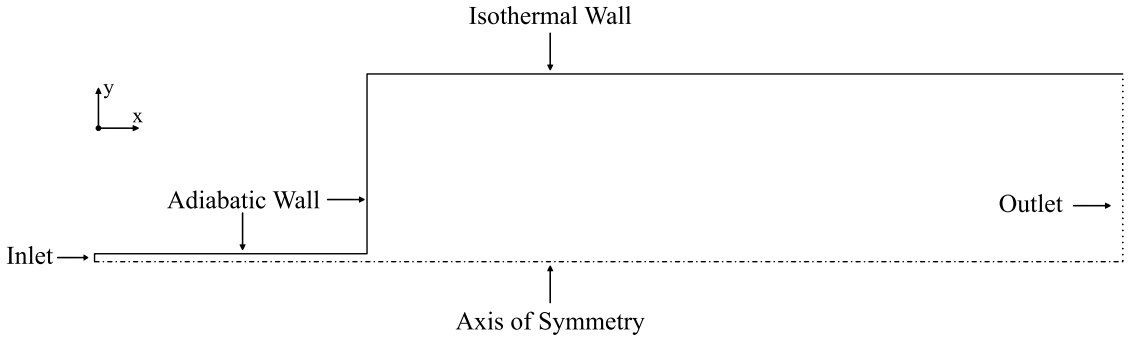

Figure 4.2: Domain boundary conditions

While section 4.2.7 is dedicated to determining the necessary mesh resolution for the present conditions, we make already a small comment on this subject. The near wall region of a flow can be divided into three main layers. Closest to the wall is the viscous sublayer where the flow is almost laminar and the molecular viscosity plays the dominant role in mass, momentum and heat transfer. Furthest away is the fully turbulent layer and in between is the log-law region where molecular and turbulence are of similar importance. To determine the boundaries of each of these layers, a coordinate normalised by the flow conditions is typically used. The y^+ as defined in equation (4.1) is a function of the friction velocity, the absolute distance to the wall, the density and the molecular viscosity.

$$y^+ = \frac{\rho u_t d}{\mu}, \quad u_t = \sqrt{\frac{t_w}{\rho}}, \quad t_w = \mu\left(\frac{\partial u}{\partial y}\right)_{y=0} \tag{4.1}$$

Traditionally, turbulence models either resolve the flow down to the viscous sublayer, in which case $y^+ \approx 1$ is desirable, or make use of wall functions to reduce the demand on mesh resolution. In this latter case, the y^+ should be set much higher and the conclusion would be that the same mesh cannot be used for turbulence models of these two different categories. To overcome this setback, the Enhanced Wall Treatment (EWT) described in [20] is activated for all the turbulence models used. With this, all solution variables are smoothly blended from their viscous sublayer formulation to their corresponding logarithmic layer formulation, depending on the mesh. Additionally, these wall functions are calibrated to cover intermediate y^+ values between 1 and 30, effectively arriving at a mesh independent formulation. Hence, more important than achieving a certain y^+ value, which is approximately 10 at the injector wall, is the overall mesh resolution inside the boundary layer. To achieve higher

quality results in this region, we set a minimum of 25 points in the wall-normal direction.

4.2.2 Boundary conditions

The domain contains five different boundary conditions displayed in Figure 4.2. At the inlet, a constant axial velocity profile is set to u_0, in accordance with the values from Table 4.1, and the radial velocity is set to zero. Additionally, the turbulent kinetic energy, turbulent dissipation rate and specific dissipation rate are based on the turbulent intensity, I, and turbulent viscosity ratio, μ_t/μ:

$$k = \frac{3}{2}(Iu_0)^2, \quad \varepsilon = \rho C_\mu \frac{k^2}{\mu}\left(\frac{\mu_t}{\mu}\right)^{-1}, \quad \omega = \rho\frac{k}{\mu}\left(\frac{\mu_t}{\mu}\right)^{-1} \tag{4.2}$$

C_μ is specific to each of the turbulence models and u_0 is the injection velocity already mentioned. In the Spalart-Allmaras model, $\tilde{\nu}$ is taken directly from the turbulent viscosity ratio, and in the Stress-BSL model the turbulent stresses are assumed to be zero, except for the trace of the tensor which is calculated as in equation (3.48). In all cases, the turbulence intensity is set to 5% at the inlet and the turbulent viscosity ratio to 10.

A pressure outlet is defined with a gauge pressure of $0\,\mathrm{MPa}$ and where the pressure values at the outlet face are calculated by averaging the specified operating pressure of p_∞, with the interior pressure. Also, at the axisymmetry axis, the value of any specific property is equalled to that of the adjacent cell.

At all walls, a no-slip condition is applied where both the normal and the tangential velocity components are set to zero. With the Spalart-Allmaras model, the modified turbulent viscosity is as well set to zero at the wall and the same happens to the Reynolds stresses in the Stress-BSL model. The remaining turbulent variables are defined using the already discussed EWT, described in [20].

Finally, for the adiabatic walls of the injector and the faceplate, the heat flux from equation (3.49) is set to zero, but for the isothermal wall heat transfer is calculated through a dirichlet boundary condition by setting a constant temperature at the wall of $297\,\mathrm{K}$:

$$q = h_f(T_w - T_f) \tag{4.3}$$

where h_f is the fluid side heat transfer coefficient, T_w is the temperature at the wall and T_f is the local fluid temperature.

4.2.3 Discretisation

FLUENT® uses a Finite Volume Method (FVM) where the integral form of an equation is calculated over the regarded domain as equation (4.12) shows. If, for example, the control volume Θ equals $\Theta_1 + \Theta_2 + \Theta_3$, the conservation equation is applied to each of the finite volumes and the internal surface fluxes must cancel each other so that only exterior contri-

butions remain. Such a property is essential for the scheme to remain conservative and an FVM approach automatically guarantees this condition.

To explain the concept behind discretisation schemes, we introduce the definition of the derivate of a function $\phi(x)$ at point x:

$$\frac{\partial \phi}{\partial x} = \lim_{\Delta x \to 0} \frac{\phi(x + \Delta x) - \phi(x)}{\Delta x} \quad (4.4)$$

By using a Taylor expansion, and for $\Delta x \neq 0$:

$$\phi(x + \Delta x) = \phi(x) + \Delta x \frac{\partial \phi}{\partial x} + \frac{\Delta x^2}{2!} \frac{\partial^2 \phi}{\partial x^2} + \frac{\Delta x^3}{3!} \frac{\partial^3 u}{\partial x^3} + \cdots \quad (4.5)$$

or

$$\frac{\phi(x + \Delta x) - \phi(x)}{\Delta x} = \frac{\partial \phi}{\partial x} + \frac{\Delta x}{2!} \frac{\partial^2 \phi}{\partial x^2} + \frac{\Delta x^2}{3!} \frac{\partial^3 \phi}{\partial x^3} + \cdots = \frac{\partial \phi}{\partial x} + O(\Delta x) \quad (4.6)$$

where the truncation error $O(\Delta x)$ goes to zero with the first power of Δx. For $O(\Delta x^2)$, the error goes to zero with second power of Δx and a first-order approximation becomes a second-order approximation.

By considering a discrete domain with a finite number of points as shown in Figure 4.3, equation (4.6) can be replaced with

$$\frac{\partial \phi_C}{\partial x} = \frac{\phi_R - \phi_C}{\Delta x_r} - \frac{\Delta x}{2!} \frac{\partial^2 \phi_C}{\partial x^2} - \frac{\Delta x^2}{3!} \frac{\partial^3 \phi_C}{\partial x^3} = \frac{\phi_R - \phi_C}{\Delta x_r} + O(\Delta x) \quad (4.7)$$

which is a first-order forward difference. A first-order backward difference can be obtained by subtracting Δx instead of adding it:

$$\frac{\partial \phi_C}{\partial x} = \frac{\phi_C - \phi_L}{\Delta x_l} + \frac{\Delta x}{2!} \frac{\partial^2 \phi_C}{\partial x^2} - \frac{\Delta x^2}{3!} \frac{\partial^3 \phi}{\partial x^3} = \frac{\phi_C - \phi_L}{\Delta x_l} + O(\Delta x) \quad (4.8)$$

Finally, a second-order central-difference results from summing up the two previous cases:

$$\frac{\partial \phi_C}{\partial x} = \frac{\phi_R - \phi_L}{\Delta x_l + \Delta x_r} - \frac{\Delta x^2}{3!} \frac{\partial^3 \phi}{\partial x^3} = \frac{\phi_R - \phi_L}{\Delta x_l + \Delta x_r} + O(\Delta x^2) \quad (4.9)$$

or

$$\frac{\partial \phi_C}{\partial x} = \frac{\phi_r - \phi_l}{\Delta x_C} + O(\Delta x^2) \quad (4.10)$$

FLUENT® stores the values of the scalar ϕ at the cell centres, but the face values ϕ_r and ϕ_l are also necessary and must be interpolated from the cell centred values, which can be done through a variety of different interpolation schemes. The number of points used and the position of each one, plays an important role in the order of accuracy of the discretisation

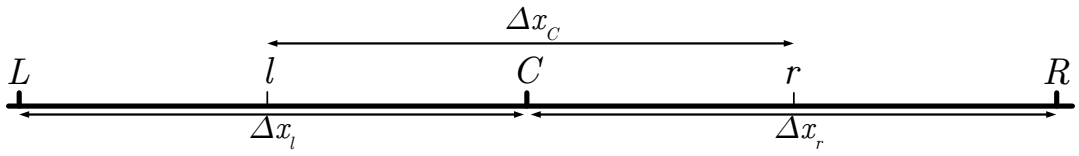

Figure 4.3: Representation of cell center values (capitalised) and face values

scheme and in how it deals with different physical phenomena. The diffusion of a certain quantity, as an example, is affected by the gradient of concentration of that same quantity over the entire domain, and a central difference is more appropriate. It is therefore used for the diffusive terms of the transport equations.

Additionally, for the advective terms, [15] demonstrates that the use of a first-order upwind scheme leads to a considerable loss of accuracy under these conditions, excluding it from our list of options. The QUICK scheme [70] is employed instead as a tool for reducing the oscillatory and unstable behaviour of second-order numerical schemes and to deal with the numerical diffusion affecting first-order upwind schemes. Equation (4.11) serves as an example to demonstrate the concept. At point C, it can be discretised using the values of ϕ at the cell faces as shown in equation (4.12). These however, need to be interpolated through the stored cell centred values.

$$\frac{\partial \phi}{\partial t} = -\frac{\partial (u\phi)}{\partial x} + \frac{\partial}{\partial x}\left(\Gamma \frac{\partial \phi}{\partial x}\right) \quad (4.11)$$

$$\frac{\partial \phi_C}{\partial t} = \left[u_l \phi_l - u_r \phi_r + \Gamma_r \left(\frac{\partial \phi_r}{\partial x}\right) - \Gamma_l \left(\frac{\partial \phi_l}{\partial x}\right)\right] / \Delta x_C \quad (4.12)$$

The application of a central differencing scheme to the diffusive term of equation (4.12) has a stabilising effect and is therefore straightforward. However, when applied to the advective term, it can lead to instabilities and to an oscillatory behaviour for a grid Péclet number (Pe) higher than two, i.e., local advection two times larger than diffusion. In short, the second-order accuracy can come at the expense of stability. By contrast, in an upwind differencing scheme, the cell centred value of ϕ is assumed to represent a cell average value and hold throughout the entire cell, meaning that the face quantities are identical to the upstream cell quantities. This technique provides an increased stability of the advective term to the variations of ϕ_C, but only because of the numerical diffusion introduced by assuming $\phi_l = \phi_L$. To diminish this numerical diffusion the grid spacing must considerably decrease, leading to a higher computational cost which is also not desirable.

The QUICK scheme introduced by [70] combines a higher order accuracy with the directional behaviour of the upwind scheme to provide additional stability for the advective term in a coarser mesh. According to the illustrations on Figure 4.4a and Figure 4.4b, the face values

are defined as

$$\phi_r = \frac{1}{2}(\phi_C + \phi_R) - \frac{1}{8}(\phi_L + \phi_R - 2\phi_C) \quad (4.13)$$

$$\phi_l = \frac{1}{2}(\phi_L + \phi_C) - \frac{1}{8}(\phi_{FL} + \phi_C - 2\phi_L) \quad (4.14)$$

Additionally, the slope of the parabola at ϕ_r is identical to the slope of the chord linking ϕ_C with ϕ_R, meaning that the gradient can be defined as in equation (4.10). Like in the upwind scheme, the direction of the interpolation is based on the velocity values. With this technique, the QUICK scheme achieves third order accuracy for the advective terms in a FVM formulation [71]. Still, in the quest for additional stability, FLUENT® implements an altered version of the QUICK scheme presented by [72] in which the $1/8$ factor from equations (4.13) and (4.14) is replaced by a solution dependent value. As a result, this is used for the advective terms in equation (4.12) while the diffusive terms are discretised with second-order accurate central differences through equation (4.10). This exemplifies the numerical schemes used in this study.

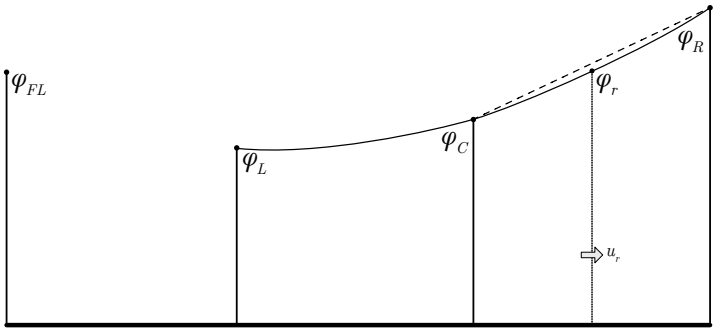

(a) Interpolation of ϕ_r

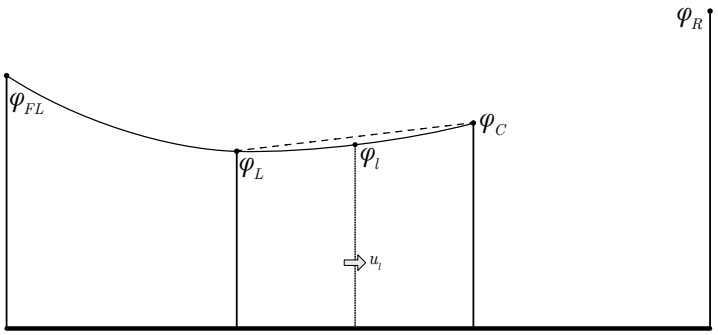

(b) Interpolation of ϕ_l

Figure 4.4: Quadratic interpolation [70]

4.2.4 Solution approach

A pressure based coupled algorithm is implemented where conservation of mass is achieved not through the continuity equation (3.8), but through a pressure based continuity equation instead. For this, the divergence operator is applied to the momentum equation (3.14) and the condition from equation (3.8) is introduced, leading to equation (4.15), that must also be averaged.

$$\frac{\partial}{\partial x_i}\left(\frac{\partial p}{\partial x_i}\right) = \frac{\partial}{\partial x_i}\left(- \rho\frac{\partial}{\partial x_j}(u_i u_j) - u_j\frac{\partial}{\partial x_j}(\rho u_i) + \frac{\partial t_{ij}}{\partial x_j} + \rho f_i\right) \quad (4.15)$$

According to this algorithm, also described in Figure 4.5, fluid properties are initially calculated through the equations described in sections 3.4, 3.5 and 3.6 with either the initial conditions or the current solution values. The turbulent viscosity is also determined at this point, after which a velocity and pressure fields need to be calculated. For this, a system of equations comprising the momentum (3.39) and the pressure based continuity equation (4.15) are solved simultaneously. After this point, the energy equation (3.51) is solved along with the transport equations for the turbulent variables introduced in section 3.3. The cycle is repeated until the condition of convergence is achieved.

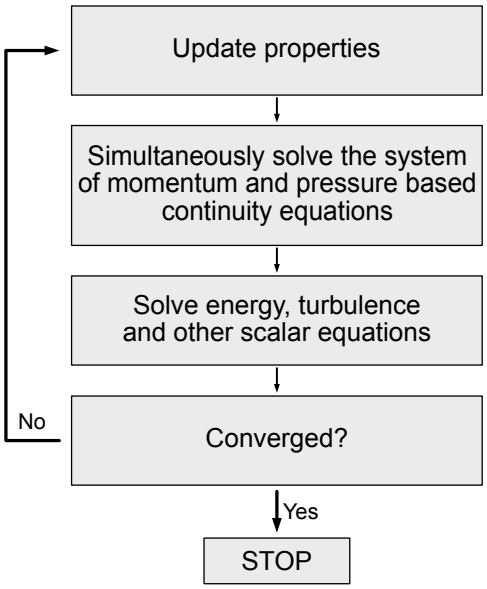

Figure 4.5: Pressure based solution algorithm

But equation (3.39) still requires the pressure values at the cell faces and these must interpolated from the cell centred values. In a collocated grid scheme, both the velocity and the pressure values needed for interpolation are retrieved from the same cell. But when calculating the pressure field with equation (4.15) on a collocated grid, oscillations in the pressure field may appear as a result of an odd-even decoupling of the pressure and velocity, i.e., that on a specific point the pressure and velocity do not affect one another. The PRESTO! (PREs-

sure STaggering Option) [20] scheme employs a staggered grid method [73] whereby the velocity and pressure values are stored in different positions and for which the control volumes are no longer equal. Ultimately, the pressure values are calculated directly for the cell face and no interpolation is needed. This results in the elimination of the decoupling of the pressure and velocity fields along with any possible oscillations and is therefore used in the current work.

4.2.5 Initialisation and convergence criteria

A hybrid initialisation method [20] is employed where the Laplacian of the velocity potential is solved,

$$\nabla^2 \varphi = 0 \quad (4.16)$$

with certain boundary conditions: the normal velocity is zero at the wall, u_0 at the inlet and the velocity potential is zero at the outlet. The pressure field is also solved using an equation similar to equation (4.16) by assuming p_∞ at the outlet as a boundary condition. These initial velocity and pressure fields are then introduced into the first iteration of the algorithm from Figure 4.5.

For the present work, convergence is assumed when the conditions for each equation in Table 4.2 are reached. The residuals are used as convergence criteria for their link to the solution error. When this tends to zero so do the residuals, [54]. This technique is necessary since the exact solution is not known and thus the solution error cannot be directly calculated.

Table 4.2: Convergence criteria

Equation	Absolute criteria
Continuity	5×10^{-4}
Momentum	1×10^{-3}
Energy	1×10^{-6}
Modified Turbulence Viscosity	1×10^{-3}
Turbulent Kinetic Energy	1×10^{-3}
Specific Dissipation Rate	1×10^{-3}
Turbulent Dissipation Rate	1×10^{-3}
Reynolds Stresses	1×10^{-3}

4.2.6 Under-relaxation

The under-relaxation of variables, usually referred to as explicit under-relaxation, reduces the change of ϕ from one iteration to the next. The under-relaxation factor θ is implemented so that

$$\phi = \phi^{old} + \theta \Delta \phi \quad (4.17)$$

where $\Delta\phi$ is the difference between the calculated solution and the solution at the previous iteration, ϕ^{old}. This means that the higher the value of θ, the higher the convergence rate should be because more weight is given to the calculated solution. On the other hand, this might increase instabilities in regions of high gradients.

Under-relaxation of equations, known as implicit relaxation, is also applied through a pseudo time step method where the term from equation (4.18) is added to the discretised equation.

$$\rho\Delta u\frac{\phi-\phi^{old}}{\Delta t} \quad (4.18)$$

In equation (4.18), Δt does not represent a physical time step but instead a pseudo time step that defines the level of relaxation.

The explicit and implicit relaxation factors used are those from Tables 4.3 and 4.4, respectively. The verification values mentioned in these two Tables are used to determine if the initially used factors have an impact on the final solution. For case 3 with the standard $k-\varepsilon$ model, we let the solution converge on these initial relaxation factors, after which we allow the calculation to restart from the last solution with the verification relaxation factors. As there is no disturbance in the residuals, it can be concluded that the relaxation has no influence on the solution. Its influence is merely felt on the speed and stability of convergence.

Table 4.3: Explicit under-relaxation factors

Variable	Initial Relaxation Factor	Verification Relaxation Factor
p	0.5	0.75
ρ	0.3	0.4
μ_t	0.5	0.75
k	0.4	0.75
ε	0.3	0.75
ω	0.4	-
$\tilde{\nu}$	0.4	-
τ_{ij}	0.5	-

Table 4.4: Implicit under-relaxation factors

Equation	Initial Relaxation Factor	Verification Relaxation Factor
Momentum	0.5	0.75
Energy	0.3	0.4

4.2.7 Independence study

A mesh independency study based on the centreline decay of the density is performed using three levels of refinement with 180 000, 280 000 and 495 000 points in a structured orthogonal mesh of rectangular elements. The comparison is made for case 4 from Table 4.1 and the results, with the standard $k-\varepsilon$ model, are shown in Figure 4.6. Despite a very slight variation of density values in the transition region, the three meshes provide close results to one another with similar slopes indicating that the flow is sufficiently well resolved with

the coarser grid. The more refined grid is not applied because the gain in accuracy does not justify the additional computational cost and the mesh of 280 000 points is used over the coarser one to maintain grid independence for the remaining turbulence models.

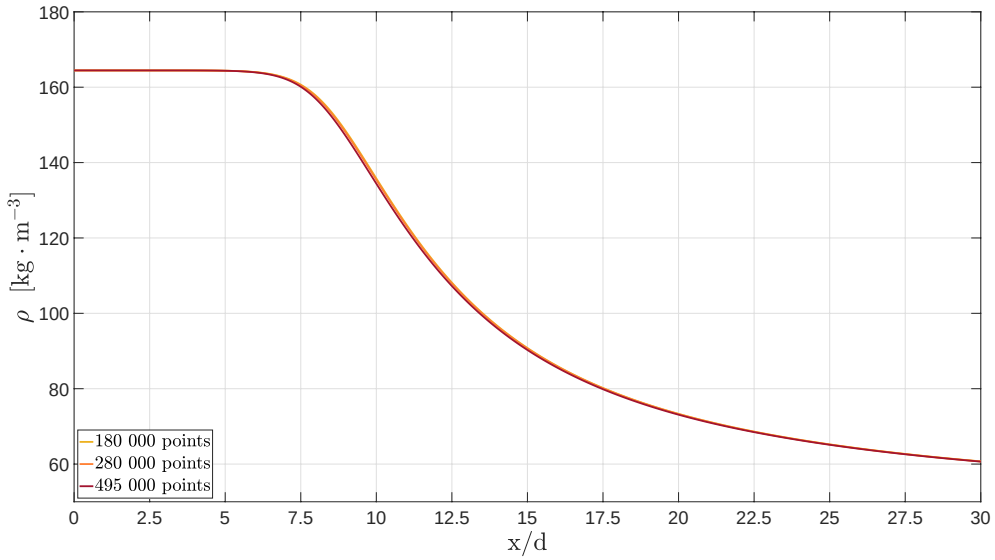

Figure 4.6: Centreline density decay at three different grid resolututions for case 4 with the standard $k-\varepsilon$ model and the REFPROPv9.1 [65]

Chapter 5

Results and Discussion

The results for the test conditions of both case 3 and 4 of [27], are presented in normalised values obtained from equation (2.2). This is especially important when comparing the results to those of other researchers since it provides a common scale for comparison. The injection and farfield density values are specific to each test and, for the present study, are listed in Table 4.1. Absolute density values are only used when comparing the results obtained through the different EoS.

5.1 Chamber

Figure 5.1 shows a comparison between the models described in section 3.3 for case 3 and case 4. [35] describes the end of the potential core region as the point at which density begins to rapidly decrease and, for the sake of comparison, we define this point at $\rho^+ = 0.99$. In Figure 5.1a we see that almost all models predict a similar length potential core with values ranging between $\mathrm{x/d} \approx 6.4$ and $\mathrm{x/d} \approx 7.6$. The only exception is the standard $k-\omega$ model that largely overestimates the length of the potential core up to $\mathrm{x/d} \approx 12.5$, which could be attributed to the poor performance of this model in free stream conditions. Even if the version here used is an improvement over the 1998 Wilcox $k-\omega$ [59] with an additional cross-diffusion term in the turbulent kinetic energy transport equation designed to improve the behaviour under free stream conditions [20], it seems to have little impact under these conditions. The poor behaviour of this model is apparent not just in the transition region but throughout the entire domain. It is as well visible that the density values in the potential core are considerably higher than those from the experimental measurements. As was already discussed in section 2.2.2, this could be attributed by the very high density inside the potential core that tends to deflect the radiation of the incident beam in the axial direction, decreasing the Raman scattering arriving at the sensor. As a result, the prediction of the density values in the potential core should be more accurate than what Figure 5.1a impresses on the reader. As the density decreases in the transition region, the radiation deflection decreases, the Raman scattering related errors diminish and the experimental data are already in better accordance with the numerical results.

Still in the potential core, turbulence seems to have no impact in the development of the jet since instabilities have not yet appeared and therefore the density remains constant. In the transition region, [28] reports a maximum in density fluctuations as pockets of injected nitrogen begin too smear out and cross the pseudo-boiling line. The same author also discusses how the heat absorbed to overcome the intermolecular attraction leads to an increase in the

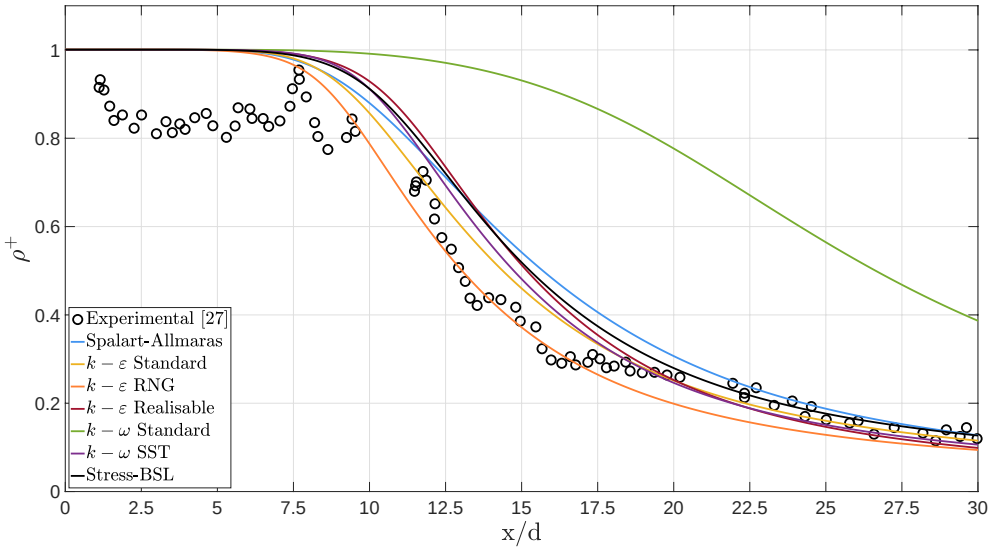

(a) Case 3

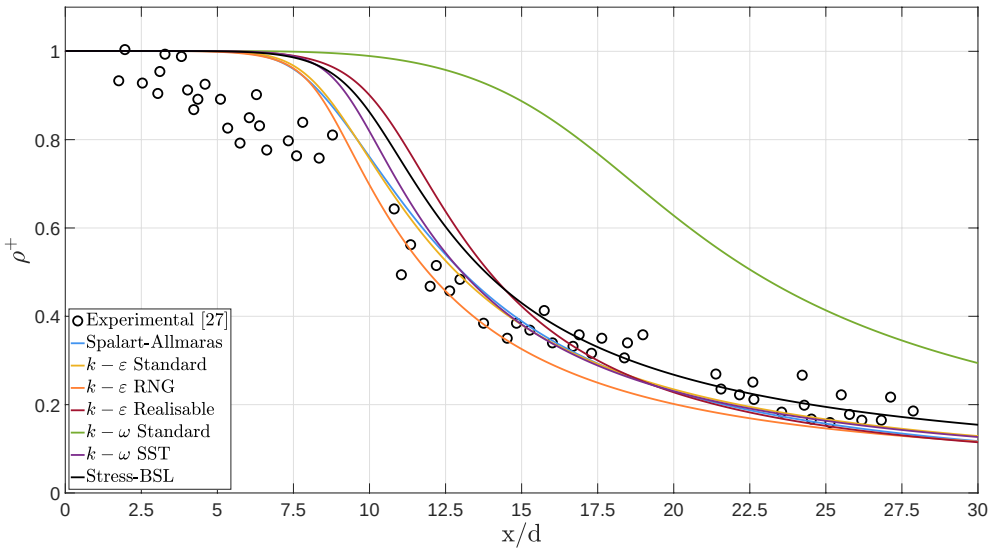

(b) Case 4

Figure 5.1: Centreline density decay with different turbulence models and the REFPROPv9.1 [65]

heat entropy production with a maximum already closer to the self-similar region. An analogy can be found between this and the trend of k and ε. Figure 5.2 shows how the dissipation rate of turbulence reaches a maximum in the transition region but begins to decrease when the fluid crosses the pseudo-boiling line, leading to thermal expansion and a reduction in shearing. In turn, this thermal expansion spawns strong variations in velocity that are visible in the increase of the turbulent kinetic energy, indicative of a stronger turbulent mixing mechanism.

With the increase of these turbulent mixing effects, the behaviour of the different models starts to diverge in the transition region. Here, the energy dissipation plays a significant role at the same time as the density values begin to sharply decrease. The more complex structure of the SST $k-\omega$ model does not provide exceptionally good results in this region, despite its

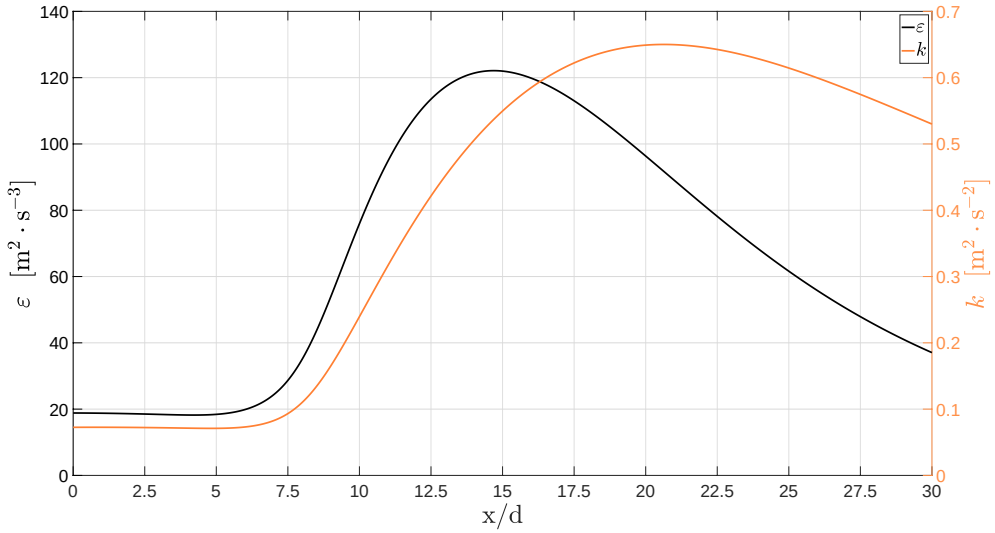

Figure 5.2: Centreline distribution of the turbulent dissipation rate and of the turbulent kinetic energy for case 3 with the RNG $k-\varepsilon$ model and the REFPROPv9.1 [65]

alternating coefficients and shear stress based formulation for μ_t. In fact, when moving away from the wall, the model only uses the $k-\varepsilon$ based coefficients and consequently we can see that its behaviour more closely matches that of the $k-\varepsilon$ than that of the standard $k-\omega$ model. Also, the additional formulation for μ_t has little impact here as it only becomes active in the near wall region. The five equation Stress-BSL model also overestimates the density values between $7.5 < \mathrm{x/d} < 20$. This can be attributed in part to the dependency of this model on ω and the inherent deficiencies of its transport equation and coefficients. However, for $\mathrm{x/d} > 20$ it is one of the models that better agrees with the experimental data. The Spalart-Allmaras model also provides slightly over estimated results between $7.5 < \mathrm{x/d} < 22.5$ but it is striking to see how well a one equation model behaves next to a five equation one.

Between the three ε based models, the realisable $k-\varepsilon$ provides the worst results right after the end of the potential core and it begins only to coincide with the experimental measures at $\mathrm{x/d} \approx 20$. At least for this case, its alternate equations for ε and C_μ equations are no improvement over the other two variants. Between the standard $k-\varepsilon$ model and the RNG version, there are two main differences: the formulation for the destruction of ε and the new definition for the turbulent Pr number inserted in the turbulent transport equations (3.70) and (3.71) and in the energy equation (3.51). Especially when considering the work from [64], we are led to believe that the variable Pr number is the main cause for the improved behaviour of the RNG $k-\varepsilon$ model over the standard version. The model accurately predicts density decay across the domain with the exception of the region between $17.5 < \mathrm{x/d} < 25$ where there is a slight under estimation. Nevertheless, from all the tested models, it is the one that provides the best results for case 3.

Finally, with the exception of the standard $k-\omega$ model, all others tend to the same values of density around $\mathrm{x/d} = 30$ where according to [27] a self-similar development is to be expected.

In case 4 the differences in potential core length, depicted in Figure 5.1b, are similar to those of case 3 ranging from $\mathrm{x/d} \approx 6.6$ to $\mathrm{x/d} \approx 7.7$, with the exception of the standard $k-\omega$ model that once again shows an ill behaviour until $\mathrm{x/d} = 30$. The injection density in this case is considerably lower than that of case 3 and the magnitude of the experimental measurements matches the numerical results right from the start. However, the unrealistic potential core discussed in section 2.3 is still predicted, independently of the model used which does not agree with the results from [27]. As [14] concludes, the more energy is needed to reach the pseudo-boiling temperature, the more stable the potential core is and this energy is considerably higher for case 3 than for case 4. The author suggests that the reduced stability of the potential in case 4 coupled with a possible heating mechanism inside the injector are sufficient to completely eliminate the potential core at the injector exit. However, the results presented in Figure 5.1b do not account for an isothermal injector wall which might be the reason for the incorrect prediction of a potential core.

In this case, the Stress-BSL model is the one to better predict the density values in $17.5 < \mathrm{x/d} < 30$ while the majority provides underestimations. Nevertheless, its behaviour outside this region is not exceptional and the overall results do not justify the computational cost. The slope produced by the SST $k-\omega$ model does not match that of the experimental data, but the results start matching the experimental data earlier than they do in case 3. A difference in behaviour is also noticeable for the ε based models. Here, the standard $k-\varepsilon$ model gives slightly better predictions in the transition region than it does for case 3. More noticeable is the resemblance between its results and those of the Spalart-Allmaras model. In this case, the RNG $k-\varepsilon$ displays a worse behaviour with results that are slightly off for $15 < \mathrm{x/d} < 22.5$, but still acceptable. Once again, by $\mathrm{x/d} = 30$ the majority of the models lead to similar values of density in the centreline where a self-similar structure is already present.

The RNG $k-\varepsilon$ provides the most reliable results for case 3 but its computational time is high when compared to the other μ_t based models, which is even more noticeable for case 4. In this instance, there is not one that greatly surpasses the others in quality of results and performance. Still, the reasonable accuracy of the Spallart-Almaras and the standard $k-\varepsilon$ models is followed by their higher efficiency when compared to the other models. The same cannot be said for the Reynolds stress model, for which the calculation time is between 5.5 and 7 times that of the most efficient for each case.

Based on the previous overall analysis, the results obtained when using the RNG $k-\varepsilon$ model are used for comparison with the results from other researchers for case 3 and 4 while the Spalart-Allmaras model is additionally used for comparison in case 4 due to its simpler formulation, reasonably accurate results and higher efficiency. This comparison is displayed in Figure 5.3 where, especially for case 3, there is a clear improvement with the RNG $k-\varepsilon$ model over LES. In fact, we can see that simpler turbulence models generally outperform LES, no matter the author. The exception to the rule are the results from [36] that are in much better agreement with the experimental data, but at a higher computational cost.

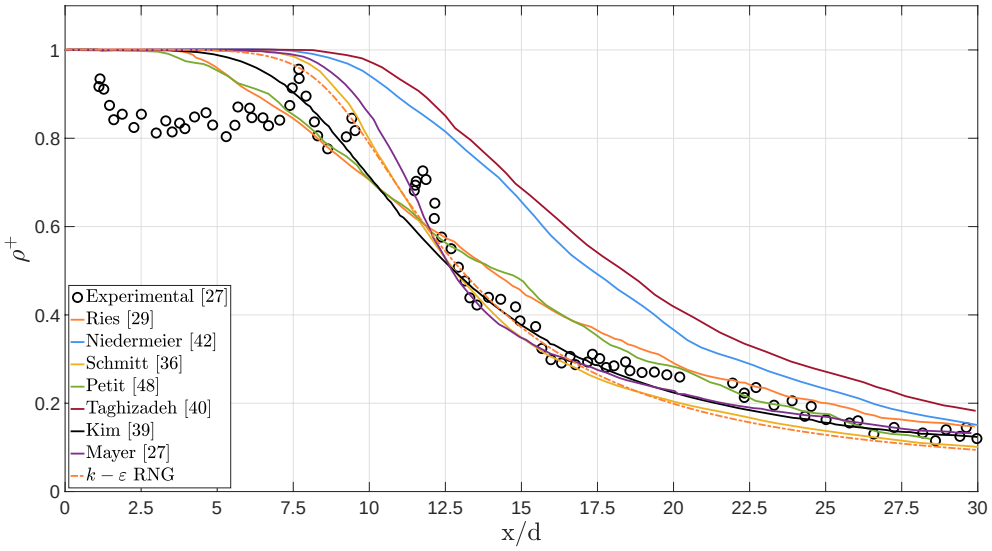

(a) Case 3

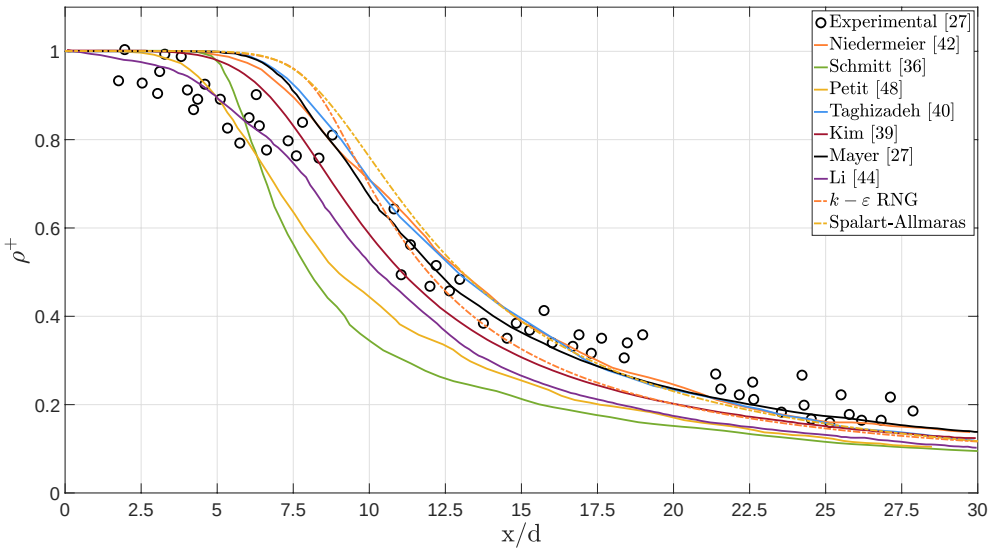

(b) Case 4

Figure 5.3: Centreline density decay comparison between different authors and the present work with the REFPROPv9.1 [65]

In case 4 the improvement is not as clear. Figure 5.3b shows that the present work provides the longest potential core while the study from [44] does not predict a potential core at all, despite not making reference to heat transfer inside the injector. For $\mathrm{x/d} > 7.5$ the results from [27, 40, 42] have the most accurate predictions while those from [36, 48] largely underestimate the density values. When comparing the results from [27] and even those with the Spalart-Allmaras model to those of [40, 42], the differences are very small at a lower computational cost. When looking at Figures 5.3a and 5.3b, there is a clear advantage in using only turbulence modelling over LES. The results are largely similar if not better and the complexity of the setup implementation and computational cost are highly diminished.

5.1.1 Equation of State influence

Moving again to the present work, Figure 5.4 shows the values for the density and specific heat obtained with the REFPROPv9.1 database, that accurately predicts the pseudo-boiling phenomenon discussed in section 2.1. In case 3, [14] shows that the injection temperature of $126.9\,\mathrm{K}$ is still below the pseudo-boiling temperature of $129.57\,\mathrm{K}$ and therefore the specific heat experiences a peak at $\mathrm{x/d} \approx 11$ as the fluid begins to warm up outside the injector. The same author also discusses the pseudo-boiling point as the point of maximum c_p and of maximum $(\partial\rho/\partial T)_p$ and Figure 5.4a matches this description showing the coincidence of both points. In case 4, the injection temperature of $137\,\mathrm{K}$ is already above the pseudo-boiling temperature and there is no peak in the specific heat. Instead, it remains fairly constant until $\mathrm{x/d} \approx 5$ along with the temperature inside the potential core, and begins then to decrease.

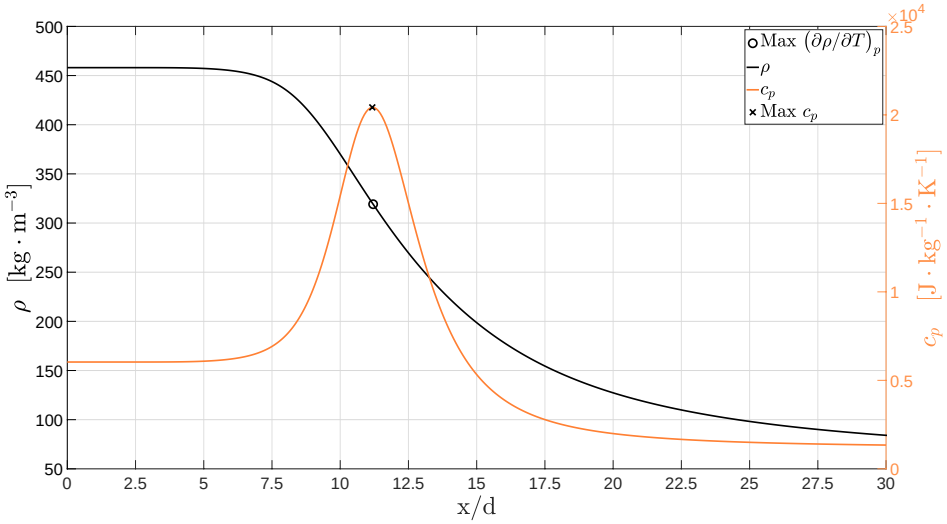

(a) Case 3

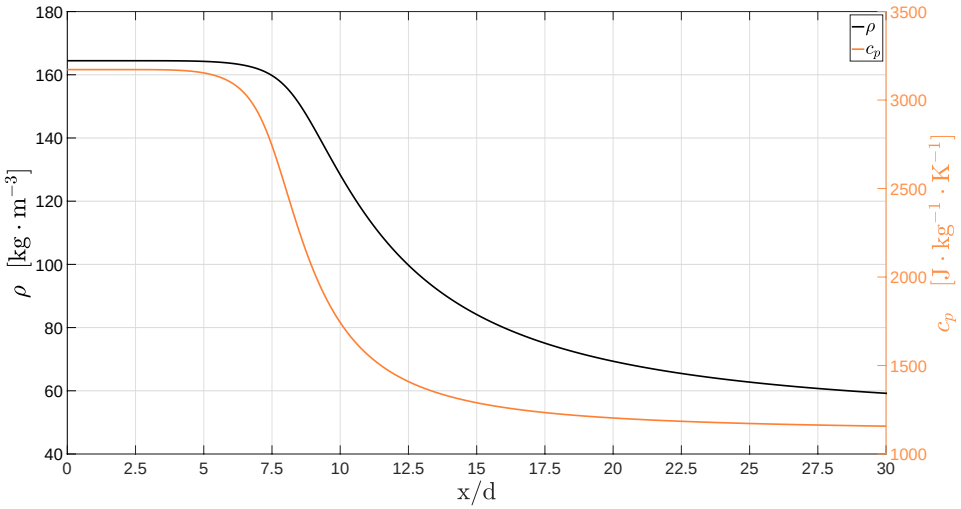

(b) Case 4

Figure 5.4: Centreline density and specific heat distribution with the RNG $k-\varepsilon$ model and the REFPROPv9.1 [65]

Also, in Figure 5.5, one can compare the influence of the three tested EoS and how they im-

pact the jet structure. In both cases, the differences are most noticeable in the potential core region. As was to be expected from Figure 3.1, the PR EoS shows better results in this region for case 3 with a relative density error of 4.6% compared to 13.4% for the SRK EoS. Even beyond the potential core, the error is significant and only begins to diminish when approaching the self-similar region where density is much reduced. Contrary to what happens in case 3, in case 4 the potential core length appears to decrease when switching from the Helmholtz energy based EoS to the cubic EoS from $\mathrm{x/d} \approx 6.6$ to $\mathrm{x/d} \approx 6$. In the potential core region, the density calculated with the PR EoS is over estimated with an error in density values relative to the Helmholtz energy EoS of 4.81% while that calculated with the SRK EoS is more accurate with a relative error of just 0.61%. In any case, beyond $\mathrm{x/d} = 10$, both the PR and the SRK EoS continue to produce a considerable amount of error which, once again, only begins to decrease around the self-similar region. One can see that the qualitative error is not as severe when plotting for ρ^+, but this goes to show how the quantitative results can be influenced by thermodynamic modelling. On top of that, despite the much improved accuracy, the efficiency when using the REFPROPv9.1 is still very much on par with that of the cubic EoS, with an average increase in computational time of only 15% when using the standard $k - \varepsilon$ model for case 4.

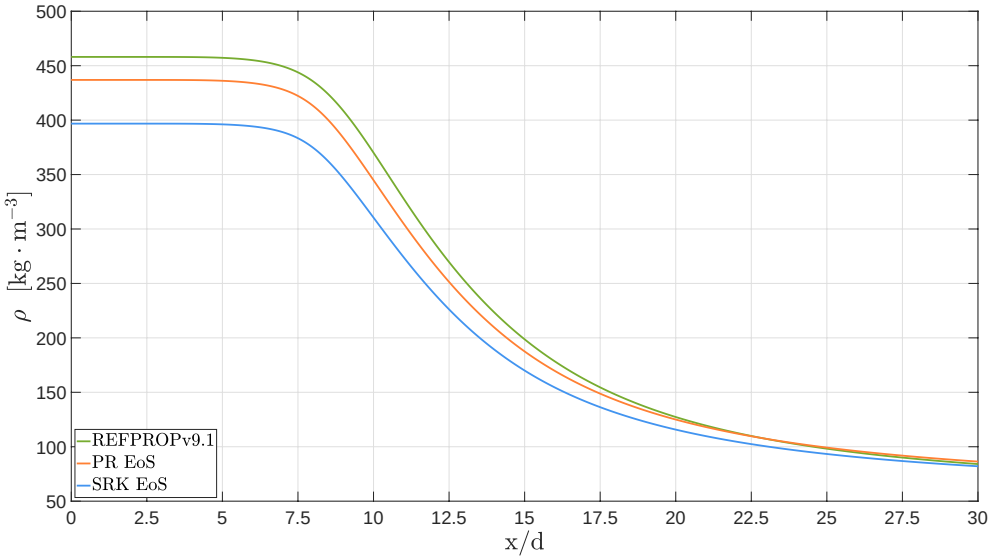

(a) Case 3

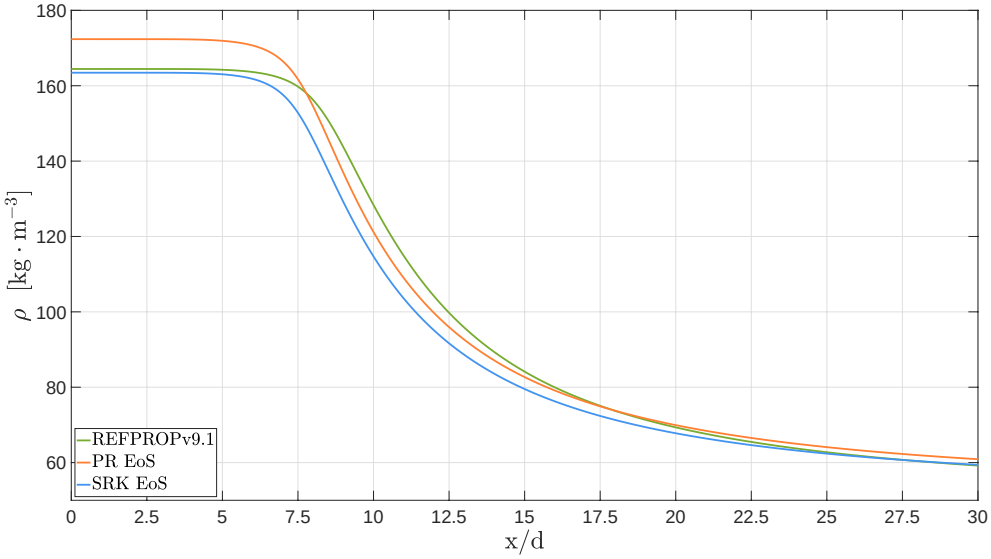

(b) Case 4

Figure 5.5: Centreline density decay with the RNG $k-\varepsilon$ model and three different EoS [21, 22, 65]

5.2 Injector

This small section is introduced to discuss the effects of the injector in the overall flow structure. While we don't consider heat transfer in this region, the length of the injector alone and the radial velocity profiles have their interest. When simulating the injector in its full length, x_i, we arrive at the centreline velocity distribution shown in Figure 5.6. As the boundary layer at the injector wall created by the no-slip condition grows with the axial coordinate, the flow near the wall slows down thus accelerating that around the axis. We can see then that at $x/x_i \approx 0.73$ the boundary layers merge together and the flow becomes completely viscous. From this point onwards, the velocity profile adjusts itself slightly to reach the fully developed turbulent velocity profile from Figure 5.7. In this figure we also make a compar-

ison to an alternate approach while setting the same constant mass flow at the inlet. When removing the injector from the domain, the power-law velocity equation [74] presented in equation (5.1) shows a good agreement with the results from the present work. Here, n is a function of the Re number, u_{max} is the axial velocity at the centreline and r is the injector radius. Such an approach constitutes a valid alternative to the simulation of the injector in terms of the velocity field effects. Since the power-law velocity equation provides very similar results to those obtained when simulating the injector, the effect on the jet structure should also be negligible.

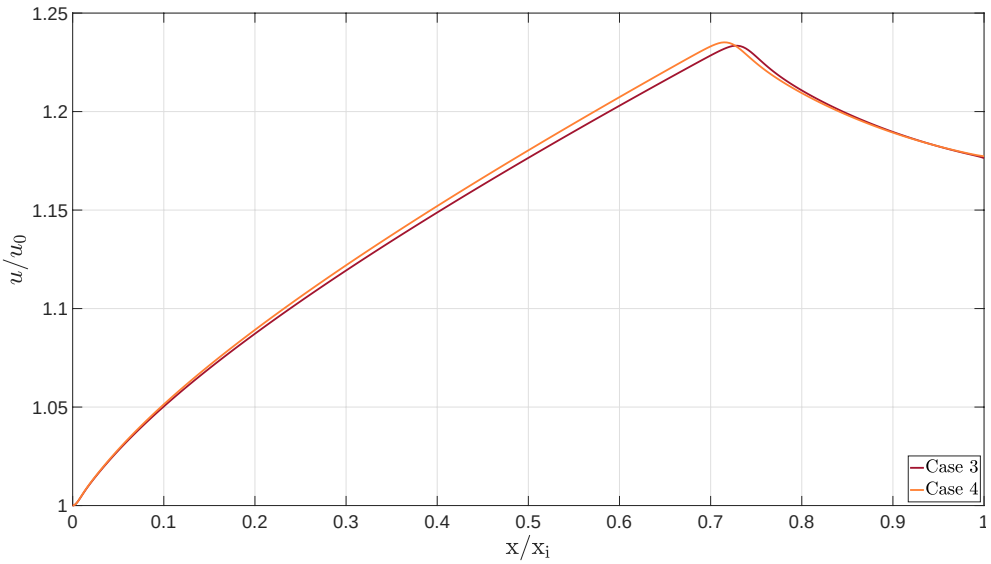

Figure 5.6: Centreline distribution of the axial velocity inside the injector for case 3 and 4 with the RNG $k-\varepsilon$ model and the REFPROPv9.1 [65]

$$\frac{u}{u_{max}} = \left(\frac{y}{r}\right)^{\frac{1}{n}} \quad (5.1)$$

Additionally, looking at both Figure 5.6 and 5.8, we can see how important the effects of the injector are and how its length influences the downstream flow. If the injector length is set to $0.75 \times x_i$, a completely viscous flow is still formed inside the injector and the flow structure inside the chamber is practically equal to when simulating with x_i. However, if the length of the simulated injector is too small and there is still an inviscid core flow at its exit, the differences become very noticeable. The effect is mainly felt in the border between the potential core and the transition region and becomes only invisible in the self-similar region.

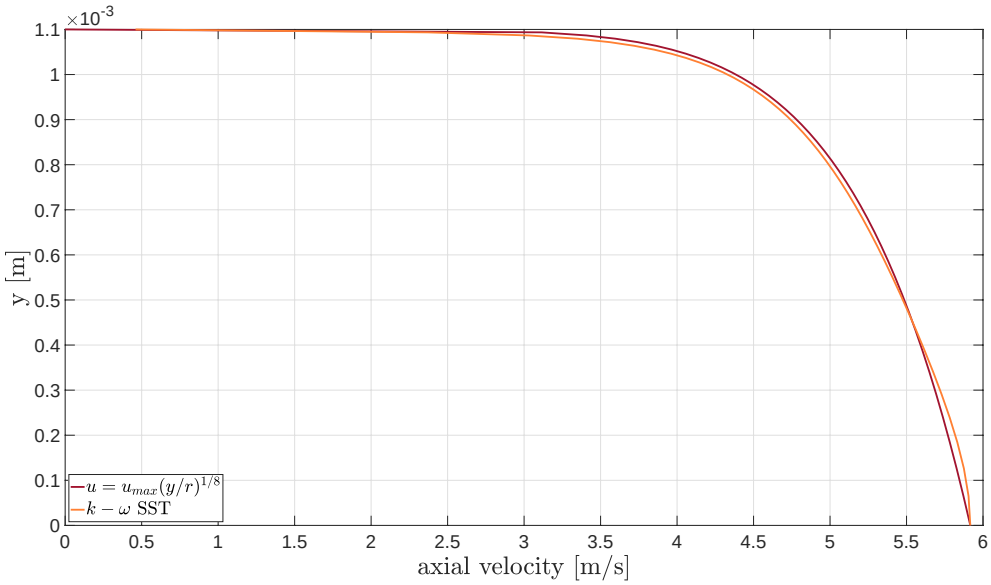

Figure 5.7: Radial distribution of the axial velocity at the injector exit for case 3 with the SST $k - \omega$ model and with the power-law velocity equation [74]

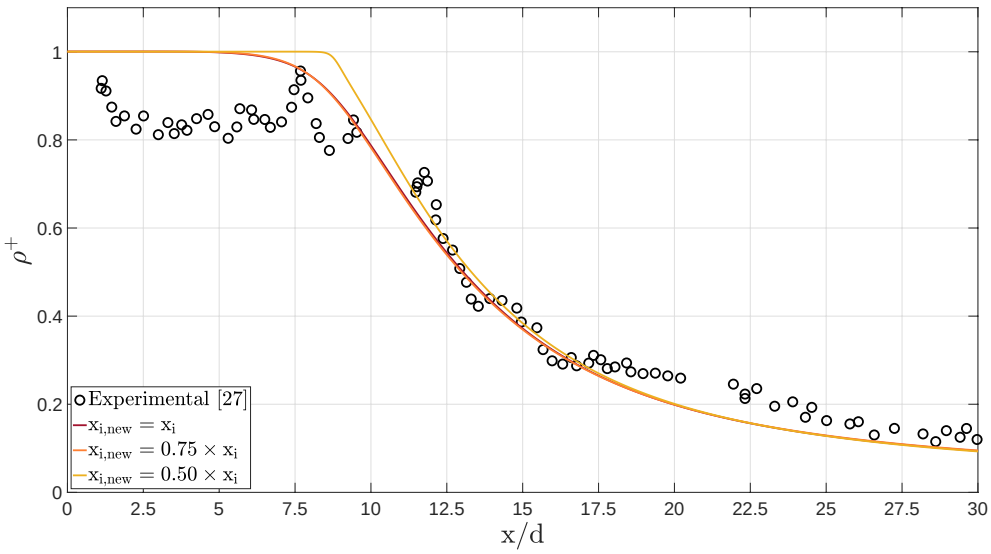

Figure 5.8: Centreline distribution of the axial velocity for case 3 with the RNG $k - \varepsilon$ model and the REFPROPv9.1 [65]

Chapter 6

Conclusions and Future Work

The steady state Favre averaged governing equations are used to deal with the incompressible but variable density flow that is characteristic of the current test cases. To study the behaviour of turbulence modelling in supercritical conditions, the system of equations is closed with seven different models, that are based either on the turbulent viscosity or on the transport of the Reynolds stresses. The effects of thermodynamic modelling are also investigated by switching between two cubic and one multi-parameter EoS. An accurate formulation is applied to the transport properties and to the isobaric specific heat. A pressure based algorithm is used where the velocity and pressure fields are solved simultaneously. A staggered grid method is then implemented to prevent pressure fluctuations together with the QUICK scheme for the advective terms and second-order central differencing scheme for the diffusive terms.

With this, the current study proposes a mathematical model that is capable of dealing with the strong temperature and density gradients typical of supercritical injections as well as with the non-linear behaviour of the thermodynamic properties. The results obtained are compared to the experimental data for validation and to additional numerical work. There is a generally good agreement with the experimental data for both case 3 with the RNG $k-\varepsilon$ model and 4 also with the RNG $k-\varepsilon$ and with the Spalart-Almaras model. Nevertheless, there is a clear distinction in the results obtained from different turbulence models. The results from the Stress-BSL model show that there is no clear advantage in calculating higher order turbulence correlation terms. The similarly complex structure of the SST $k-\omega$ model is as well not applicable to the current case and does not produce any improvements in the freestream region, over the ε based models. The RNG $k-\varepsilon$ model produces especially good results for case 3, possibly due to the variable Pr_t number but the similarly good results obtained for case 4 with the standard $k-\varepsilon$ and the Spalart-Allmaras models indicate that this might not be the only relevant factor. Besides the analysis of the axial density decay, it would be interesting in the future to look into the jet divergence angle predictions through different methods such as the FWHM. These measurements could then be compared to empirical models and experimental data to provide some additional insight into the influence of turbulence modelling on the jet structure, more specifically the shear layer.

This study strongly supports the case that there is no direct correlation between the complexity of a turbulence model and the accuracy of the final results. This argument becomes even more evident when comparing our results with those of LES from other researchers. With some exceptions, it is demonstrated that at least for case 3 the ε based models perform better

than LES. For case 4, both methods are on par with each other, but surely with an evident gap in computational cost.

An additional contribution of this study is the insight regarding the simulation of the injector. The influence of the velocity field at the exit of the injector is studied and it is shown that as long as there is still an inviscid potential core at this position, the downstream jet structure is noticeably affected. It is, therefore, a point that deserves some attention. In the end, we compare the velocity profiles produced in the present work with those of the power-law velocity equation to conclude that the latter is a good solution to replace the effects of the no-slip condition on the injector wall.

Finally, a comparison of results when using two different cubic EoS and a reference EoS for nitrogen shows how, despite the resemblance in qualitative behaviour, the quantitative results are greatly affected. The potential core density values for case 3 are better approximated with the PR EoS and the same happens for case 4 with the SRK EoS. Besides the differences in the predicted injection density, there is as well an influence on the transition region which becomes less noticeable only when approaching the self-similar region.

On a final note, the use of cubic EoS in case 4 apparently also results in a slightly smaller potential core. This potential core should not be present in the first place, but it is predicted independently of the turbulence model and the EoS that is used. Researchers have suggested that the disregard for the heating mechanism inside the injector could be in the source of the wrongfully predicted potential core and [14] obtains results with a similar slope to that of the experimental data but at lower density values. During the experimental procedure, as the nitrogen is injected, its temperature increases while that of the injector wall decreases. However, the values of the injector wall temperature at the moment when the Raman images are collected are not published. An incorrect setting of the injector wall temperature could therefore be the cause for the lower than expected density values.

Having validated the current mathematical model and determined how the velocity field affects the flow structure, one of the next steps is to determine the impact of a heating mechanism inside the injector and the boundary conditions to be used when simulating said mechanism. Once the thermal influence of the injector in the injected nitrogen is accurately simulated and validated against the experimental data, a function could be used to approximate the temperature profile at the injector exit. This would allow for the complete removal of the injector from the computational domain. Once this is achieved, the transition to the simulation of reactive mixtures may begin.

Bibliography

[1] Lockwood, J. and Hazlett, R., *Volcanoes: Global Perspectives*, Wiley-Blackwell, Oxford, England, 1st ed., 2010. 1

[2] Esposito, W., *Venus II: Geology, Geophysics, Atmosphere, and Solar Wind Environment*, University of Arizona Press, Tucson, Arizona, 1997. 1

[3] Lebonnois, S. and Schubert, G., "The deep atmosphere of Venus and the possible role of density-driven separation of CO2 and N2," *Nature Geoscience*, Vol. 10, No. 7, jun 2017, pp. 473–477. 1

[4] Brunner, G., "Applications of Supercritical Fluids," *Annual Review of Chemical and Biomolecular Engineering*, Vol. 1, No. 1, jun 2010, pp. 321–342. 1

[5] Lacaze, G., Misdariis, A., Ruiz, A., and Oefelein, J., "Analysis of high-pressure Diesel fuel injection processes using LES with real-fluid thermodynamics and transport," *Proceedings of the Combustion Institute*, Vol. 35, No. 2, 2015, pp. 1603–1611. 1

[6] Dahms, R., Manin, J., Pickett, L., and Oefelein, J., "Understanding high-pressure gas-liquid interface phenomena in Diesel engines," *Proceedings of the Combustion Institute*, Vol. 34, No. 1, jan 2013, pp. 1667–1675. 1, 9

[7] Cornelisse, J., Schoeyer, H., and Wakker, K., *Rocket Propulsion and Spaceflight Dynamics*, Pitman, London, England, 1979. 1

[8] *RS-25 Propulsion System*, Aerojet Rocketdyne, Los Angeles, California, March 2019. 2

[9] Coulon, D., *ESA Bulletin*, No. 102, European Space Agency, Noordwijk, Netherlands, May 2000. 2

[10] Haeseler, D., Haidinger, F., Brummer, L., Haberle, J., and Luger, P., "Development and Testing Status of the Vinci Thrust Chamber," *48th AIAA/ASME/SAE/ASEE Joint Propulsion Conference & Exhibit*, American Institute of Aeronautics and Astronautics, jul 2012. 2

[11] Oschwald, M., Smith, J., Branam, R., Hussong, J., Schik, A., Chehroudi, B., and Talley, D., "Injection of Fluids into Supercritical Environments," *Combustion Science and Technology*, Vol. 178, No. 1-3, jan 2006, pp. 49–100. 2, 6, 9

[12] Bellan, J., "Theory, modeling and analysis of turbulent supercritical mixing," *Combustion Science and Technology*, Vol. 178, No. 1-3, jan 2006, pp. 253–281. 5

[13] Banuti, D., Raju, M., Ma, P., Ihme, M., and Hickey, J., "Seven questions about supercritical fluids - towards a new fluid state diagram," *55th AIAA Aerospace Sciences Meeting*, American Institute of Aeronautics and Astronautics, jan 2017. 6

[14] Banuti, D., *Thermodynamic Analysis and Numerical Modeling of Supercritical Injection*, Phd thesis, University of Stuttgart, 2015. 6, 7, 8, 9, 10, 14, 15, 60, 62, 68

[15] Park, T., "LES and RANS simulations of cryogenic liquid nitrogen jets," *The Journal of Supercritical Fluids*, Vol. 72, dec 2012, pp. 232–247. 7, 14, 15, 50

[16] Younglove, B., "Thermophysical properties of fluids. I. Argon, ethylene, parahydrogen, nitrogen, nitrogen rifluoride and oxygen," 1982. 8

[17] Span, R. and Wagner, W., "Equations of State for Technical Applications. I. Simultaneously Optimized Functional Forms for Nonpolar and Polar Fluids," *International Journal of Thermophysics*, Vol. 24, No. 1, 2003, pp. 1–39. 8

[18] Span, R., Lemmon, E., Jacobsen, R., and Wagner, W., "A Reference Quality Equation of State for Nitrogen," *International Journal of Thermophysics*, Vol. 19, No. 4, 1998, pp. 1121–1132. 8

[19] Span, R., Lemmon, E., Jacobsen, R., Wagner, W., and Yokozeki, A., "A Reference Equation of State for the Thermodynamic Properties of Nitrogen for Temperatures from 63.151 to 1000 K and Pressures to 2200 MPa," *Journal of Physical and Chemical Reference Data*, Vol. 29, No. 6, nov 2000, pp. 1361–1433. 8, 37, 39, 42

[20] *ANSYS® FLUENT® Theory Guide*, Ansys Inc., Canonsburg, Pennsylvania, 2019, Release 19.1. 8, 19, 27, 28, 29, 30, 31, 32, 33, 34, 35, 36, 42, 47, 48, 53, 57

[21] Soave, G., "Equilibrium constants from a modified Redlich-Kwong equation of state," *Chemical Engineering Science*, Vol. 27, No. 6, jun 1972, pp. 1197–1203. 8, 37, 64

[22] Peng, D. and Robinson, D., "A New Two-Constant Equation of State," *Industrial & Engineering Chemistry Fundamentals*, Vol. 15, No. 1, Feb. 1976, pp. 59–64. 8, 38, 64

[23] Yang, V., "Modeling of supercritical vaporization, mixing, and combustion processes in liquid-fueled propulsion systems," *Proceedings of the Combustion Institute*, Vol. 28, No. 1, jan 2000, pp. 925–942. 9

[24] Benedict, M., Webb, G., and Rubin, L., "An Empirical Equation for Thermodynamic Properties of Light Hydrocarbons and Their Mixtures I. Methane, Ethane, Propane and n-Butane," *The Journal of Chemical Physics*, Vol. 8, No. 4, apr 1940, pp. 334–345. 9

[25] Bellan, J., "Supercritical (and subcritical) fluid behavior and modeling: drops, streams, shear and mixing layers, jets and sprays," *Progress in Energy and Combustion Science*, Vol. 26, No. 4-6, aug 2000, pp. 329–366. 9

[26] Chehroudi, B., Talley, D., and Coy, E., "Visual characteristics and initial growth rates of round cryogenic jets at subcritical and supercritical pressures," *Physics of Fluids*, Vol. 14, No. 2, feb 2002, pp. 850–861. 10, 13, 14

[27] Mayer, W., Telaar, J., Branam, R., Schneider, G., and Hussong, J., "Raman Measurements of Cryogenic Injection at Supercritical Pressure," *Heat and Mass Transfer*, Vol. 39, No. 8-9, jul 2003, pp. 709–719. 10, 11, 13, 14, 15, 16, 17, 45, 46, 47, 57, 59, 60, 61

[28] Ries, F., Janicka, J., and Sadiki, A., "Thermal Transport and Entropy Production Mechanisms in a Turbulent Round Jet at Supercritical Thermodynamic Conditions," *Entropy*, Vol. 19, No. 8, aug 2017, pp. 404. 10, 14, 57

[29] Ries, F., Obando, P., Shevchuck, I., Janicka, J., and Sadiki, A., "Numerical analysis of turbulent flow dynamics and heat transport in a round jet at supercritical conditions," *International Journal of Heat and Fluid Flow*, Vol. 66, aug 2017, pp. 172–184. 10, 14

[30] Merzkirch, W., *Flow Visualization*, Academic Press, Orlando, Florida, 2nd ed., 1987. 11, 12

[31] Raman, C. and Krishnan, K., "A New Type of Secondary Radiation," *Nature*, Vol. 121, No. 3048, mar 1928, pp. 501–502. 12

[32] Oschwald, M. and Schik, A., "Supercritical nitrogen free jet investigated by spontaneous Raman scattering," *Experiments in Fluids*, Vol. 27, No. 6, nov 1999, pp. 497–506. 12, 13

[33] Chehroudi, B., Cohn, R., Talley, D., and Badakhshan, A., "Raman scattering measurements in the initial region of sub- and supercritical jets," *36th AIAA/ASME/SAE/ASEE Joint Propulsion Conference and Exhibit*, American Institute of Aeronautics and Astronautics, jul 2000. 13, 14

[34] Mayer, W., Telaar, J., Branam, R., Schneider, G., and Hussong, J., "Characterization of cryogenic injection at supercritical pressure," *37th Joint Propulsion Conference and Exhibit*, American Institute of Aeronautics and Astronautics, jul 2001. 13, 14, 36

[35] Branam, R. and Mayer, W., "Characterization of Cryogenic Injection at Supercritical Pressure," *Journal of Propulsion and Power*, Vol. 19, No. 3, may 2003, pp. 342–355. 14, 57

[36] Schmitt, T., Selle, L., Cuenot, B., and Poinsot, T., "Large-Eddy Simulation of transcritical flows," *Comptes Rendus Mécanique*, Vol. 337, No. 6-7, jun 2009, pp. 528–538. 14, 15, 16, 60, 61

[37] Schmitt, T., Selle, L., Ruiz, A., and Cuenot, B., "Large-Eddy Simulation of Supercritical-Pressure Round Jets," *AIAA Journal*, Vol. 48, No. 9, sep 2010, pp. 2133–2144. 14, 15

[38] Hickey, J., Ma, P., Ihme, M., and Thakur, S., "Large Eddy Simulation of Shear Coaxial Rocket Injector: Real Fluid Effects," *49th AIAA/ASME/SAE/ASEE Joint Propulsion Conference*, American Institute of Aeronautics and Astronautics, jul 2013. 14

[39] Kim, T., Kim, Y., and Kim, S., "Numerical study of cryogenic liquid nitrogen jets at supercritical pressures," *The Journal of Supercritical Fluids*, Vol. 56, No. 2, mar 2011, pp. 152–163. 14, 15

[40] Taghizadeh, S. and Jarrahbashi, D., "Proper Orthogonal Decomposition Analysis of Turbulent Cryogenic Liquid Jet Injeciton Under Transcritical and Supercritical Conditions," *Atomization and Sprays*, Vol. 28, No. 10, 2018, pp. 875–900. 14, 15, 61

[41] Mueller, H., Niedermeier, C., Jarczyk, M., Pfitzner, M., Hickel, S., and Adams, N., "Large-eddy simulation of trans- and supercritical injection," *Progress in Propulsion Physics*, edited by M. Calabro, L. DeLuca, S. Frolov, L. Galfetti, and O. Haidn, EDP Sciences, 2016. 14, 15

[42] Niedermeier, C., Jarczyk, M., Hickel, S., Adams, N., and Pfitzner, M., "Large-Eddy Simulation of Turbulent Trans- and Supercritical Mixing," *21st AIAA Computational Fluid Dynamics Conference*, American Institute of Aeronautics and Astronautics, jun 2013. 14, 15, 16, 17, 61

[43] Jarczyk, M. and Pfitzner, M., "Large Eddy Simulation of Supercritical Nitrogen Jets," *50th AIAA Aerospace Sciences Meeting including the New Horizons Forum and Aerospace Exposition*, American Institute of Aeronautics and Astronautics, jan 2012. 14, 15

[44] Li, L., Xie, M., Wei, W., Jia, M., and Liu, H., "Numerical investigation on cryogenic liquid jet under transcritical and supercritical conditions," *Cryogenics*, Vol. 89, jan 2018, pp. 16–28. 14, 15, 61

[45] Terashima, H., Kawa, S., and Yamanishi, N., "High-Resolution Numerical Method for Supercritical Flows with Large Density Variations," *AIAA Journal*, 2011. 14

[46] Sierra-Pallares, J., Parra-Santos, M., García-Serna, J., Castro, F., and Cocero, M., "Numerical analysis of high-pressure fluid jets: Application to RTD prediction in supercrit-

ical reactors," *The Journal of Supercritical Fluids*, Vol. 49, No. 2, jun 2009, pp. 249–255. 14, 15

[47] Chung, T., Ajlan, M., Lee, L., and Starling, K., "Generalized multiparameter correlation for nonpolar and polar fluid transport properties," *Industrial & Engineering Chemistry Research*, Vol. 27, No. 4, apr 1988, pp. 671–679. 14

[48] Petit, X., Ribert, G., Lartigue, G., and Domingo, P., "Large-eddy simulation of supercritical fluid injection," *The Journal of Supercritical Fluids*, Vol. 84, dec 2013, pp. 61–73. 15, 16, 61

[49] Lemmon, E., McLinden, M., and Huber, M., "NIST Standard Reference Database 23 - NIST Thermodynamic and Transport Properties REFPROP, Version 7.0," July 2002. 15, 38, 39, 45

[50] Yang, Z. and Shih, T., "New time scale based k-epsilon model for near-wall turbulence," *AIAA Journal*, Vol. 31, No. 7, jul 1993, pp. 1191–1198. 15

[51] Launder, B. and Spalding, D., *Lectures in Mathematical Models of Turbulence*, Academic Press, London, England, 1972. 15, 29

[52] Barata, J., Silva, A., and Gökalp, I., "Numerical study of cryogenic jets under supercritical conditions," *40th AIAA Aerospace Sciences Meeting & Exhibit*, American Institute of Aeronautics and Astronautics, jan 2002. 15

[53] Spalart, P. and Allmaras, S., "A one-equation turbulence model for aerodynamic flows," jan 1992. 15, 27

[54] Hirsch, C., *Numerical Computation of Internal and External Flows*, Vol. 1, Elsevier, Burlington, Massachusetts, 2nd ed., 2007. 53

[55] Cebeci, T., *Analysis of Turbulent Flows with Computer Programs*, Elsevier, Oxford, England, 3rd ed., 2013. 24

[56] Wilcox, D., *Turbulence Modeling for CFD*, DCW Industries, La Cãnada, California, 3rd ed., 2006. 32

[57] Shih, T., Liou, W., Shabbir, A., Yang, Z., and Zhu, J., "A new k-ε eddy viscosity model for high reynolds number turbulent flows," *Computers & Fluids*, Vol. 24, No. 3, mar 1995, pp. 227–238. 29, 31

[58] Yakhot, V., Orszag, S., Thangam, S., Gatski, T., and Speziale, C., "Development of turbulence models for shear flows by a double expansion technique," *Physics of Fluids A:*

Fluid Dynamics, Vol. 4, No. 7, jul 1992, pp. 1510–1520. 30

[59] Wilcox, D., *Turbulence Modeling for CFD*, DCW Industries, La Cãnada, California, 2nd ed., 1998. 32, 57

[60] Menter, F., "Two-equation eddy-viscosity turbulence models for engineering applications," *AIAA Journal*, Vol. 32, No. 8, aug 1994, pp. 1598–1605. 33, 35

[61] Hanjalić, K. and Launder, B., "Contribution towards a Reynolds-stress closure for low-Reynolds-number turbulence," *Journal of Fluid Mechanics*, Vol. 74, No. 4, apr 1976, pp. 593–610. 35

[62] Lien, F. and Leschziner, M., "Assessment of turbulence-transport models including non-linear RNG eddy-viscosity formulation and second-moment closure for flow over a backward-facing step," *Computers & Fluids*, Vol. 23, No. 8, nov 1994, pp. 983–1004. 35

[63] Launder, B., Reece, G., and Rodi, W., "Progress in the development of a Reynolds-stress turbulence closure," *Journal of Fluid Mechanics*, Vol. 68, No. 3, apr 1975, pp. 537–566. 35

[64] Magalhães, L., Antunes, E., Silva, A., and Barata, J., "Cubic and multiparameter equations of state evaluation for supercritical flow modeling," *4th Thermal and Fluids Engineering Conference (TFEC)*, , No. TFEC-2019-28385, 2019. 36, 59

[65] E. Lemmon, M. Huber, M. M., "NIST Standard Reference Database 23: Reference Fluid Thermodynamic and Transport Properties-REFPROP, Version 9.1," May 2013. 37, 55, 58, 59, 61, 62, 64, 65, 66

[66] Redlich, O. and Kwong, J., "On the Thermodynamics of Solutions. V. An Equation of State. Fugacities of Gaseous Solutions." *Chemical Reviews*, Vol. 44, No. 1, feb 1949, pp. 233–244. 37

[67] Pfennig, A., *Thermodynamik der Gemische*, Springer, New York, New York, 2004. 38

[68] Lemmon, E. and Jacobsen, R., "Viscosity and Thermal Conductivity Equations for Nitrogen, Oxygen, Argon, and Air," *International Journal of Thermophysics*, Vol. 25, No. 1, jan 2004, pp. 21–69. 39, 40, 41

[69] Branam, R., Telaar, J., and Mayer, W., "Simulation of Cryogenic Jet Injection, RCM 1," *2nd International Workshop on Rocket Combustion Modeling: Atomization, Combustion and Heat Transfer*, 2001. 45

[70] Leonard, B., "A stable and accurate convective modelling procedure based on quadratic upstream interpolation," *Computer Methods in Applied Mechanics and Engineering*, Vol. 19, No. 1, jun 1979, pp. 59–98. 50, 51

[71] Leonard, B., "Order of accuracy of QUICK and related convection-diffusion schemes," *Applied Mathematical Modelling*, Vol. 19, No. 11, nov 1995, pp. 640–653. 51

[72] Leonard, B. and Mokhtari, S., "ULTRA-SHARP Nonoscillatory Convection Schemes for High-Speed Steady Multidimensional Flow," 1990. 51

[73] Patankar, S., *Numerical Heat Transfer and Fluid Flow*, Hemisphere, Washington, D.C., Washington, 1980. 53

[74] Cengel, Y. and Cibala, J., *Fluid Mechanics: Fundamentals and Applications*, McGraw-Hill, New York, New York, 2006. 65, 66